

# The Dusty Heart of NGC 4151 Revealed by $\lambda \sim 1\text{--}40 \mu\text{m}$ Reverberation Mapping and Variability: A Challenge to Current Clumpy Torus Models

JIANWEI LYU (吕建伟)<sup>1</sup> AND GEORGE H. RIEKE<sup>1</sup>

<sup>1</sup> *Steward Observatory, University of Arizona, 933 North Cherry Avenue, Tucson, AZ 85721, USA*

## ABSTRACT

We probe the dusty environment of the archetypical type-1 AGN in NGC 4151 with comprehensive IR reverberation mapping over several decades, in J ( $\sim 1.22 \mu\text{m}$ ), H ( $\sim 1.63 \mu\text{m}$ ), K ( $\sim 2.19 \mu\text{m}$ ), L ( $\sim 3.45 \mu\text{m}$ ) and N-band ( $\sim 10.6 \mu\text{m}$ ), plus multiple measurements at  $20\text{--}40 \mu\text{m}$ . At  $1\text{--}4 \mu\text{m}$ , the hot dust reverberation signals come from two distinct dust populations at separate radii ( $\sim 0.033 \text{ pc}$  and  $\sim 0.076 \text{ pc}$ ), with temperatures of  $\sim 1500\text{--}2500 \text{ K}$  and  $\sim 900\text{--}1000 \text{ K}$ , consistent with the expected properties of sublimating graphite and silicate dust grains. The domination of the torus infrared output by carbon and silicate grains near their sublimation temperatures and radii may account for the general similarity of AGN near-IR spectral energy distributions. The torus inner edge defined by the hottest dust remains at roughly the same radius independent of the AGN optical luminosity over  $\sim 25$  years. The emission by hot dust warmed directly by the optical/UV AGN output has increased gradually by  $\sim 4\%$ /year, indicating a possibly growing torus. A third dust component at  $\sim 700 \text{ K}$  does not seem to participate directly in the IR reverberation behavior and its emission may originate deep in the circumnuclear torus. We find a reverberation signal at  $\sim 10 \mu\text{m}$  with an inferred radius for the warm dust of  $\sim 2.2\text{--}3.1 \text{ pc}$ . The lack of variability at  $20\text{--}40 \mu\text{m}$  indicates the far-IR emission comes from even more extended regions. The torus properties revealed by dust reverberation analysis are inconsistent with predictions from pure clumpy torus models. Instead, the longer wavelength emission possibly originates in a flared torus or the polar wind.

*Keywords:* galaxies:active — galaxies:Seyfert — quasars:general — infrared:galaxies — dust, extinction

## 1. INTRODUCTION

Circumnuclear dusty structures and their accompanying obscuration are essential characteristics of the active galactic nucleus (AGN) phenomenon (e.g., Antonucci 1993; Urry & Padovani 1995; Netzer 2015) and are possibly tightly linked to the growth and evolution of the accreting supermassive black holes (SMBH) (e.g., Hopkins et al. 2012; Wada 2012; Wang et al. 2017). Current models for AGN obscuration are centered on an optically-thick torus-like circumnuclear structure that absorbs optical/UV light from the central engine and reradiates it at infrared (IR) wavelengths (e.g., Fritz et al. 2006; Nenkova et al. 2008a,b; Stalevski et al. 2016) and have achieved some success in matching the infrared observations (e.g., Nenkova et al. 2008b; Ramos Almeida et al. 2009, 2011; Alonso-Herrero et al. 2011). Dusty winds launched from this torus may also play a major role (Hönig et al. 2013). However, due to the lack of spatially-resolved direct observations, the inferred properties of the torus, such as its geometric structure and temporal evolution, are highly ambiguous (e.g., González-Martín et al. 2019).

Luckily, this compact dust structure can be probed by time-domain observations. Depending on the AGN luminosity and observed wavelength, the circumnuclear torus ranges from light-weeks to many light-years in size. When the energy output of the nucleus varies, the signals we receive encode the torus structure as a result of the light travel times from the

central engine to the reradiating zone and then to us. Thus, cross-correlation analysis of the AGN optical and IR light curves, i.e. dust reverberation analysis, provides a powerful tool to pin down the torus structures (e.g., Clavel et al. 1989; Barvainis 1992; Suganuma et al. 2006; Koshida et al. 2014; Lyu et al. 2019). Most such studies are focused on the K-band (at  $2.2 \mu\text{m}$ ), which can be easily accessed with ground-based observations (e.g., Koshida et al. 2014; Minezaki et al. 2019). Multi-band reverberation behavior can reveal additional aspects of the circumnuclear torus structure (e.g., smooth, clumpy, some combination). However, there are relatively few such explorations and the available studies show a range of results (e.g., Glass 2004; Oknyansky et al. 2014; Lyu et al. 2019). It is also hypothesized that the circumnuclear torus should change structure in reaction to changing nuclear luminosity resulting in changes in the reverberation timing, but again there is a range of results (e.g., Oknyansky et al. 2014; Schnülle et al. 2015).

As one of the brightest and nearest type-1 AGN, NGC 4151 has been extensively observed at multiple wavelengths, offering the opportunity to explore these issues with optical and IR data collected over 40 years. It has been, by far, the most extensively studied AGN by means of IR reverberation mapping (e.g., Oknyanskii 1993; Oknyansky et al. 2014, 2019; Koshida et al. 2014; Schnülle et al. 2015). These studies have generally used a subset of the available data

and have often reached contradictory results (e.g., Koshida et al. 2009; Hönig & Kishimoto 2011). To clarify the inner torus properties in NGC 4151, we have conducted a comprehensive dust reverberation mapping analysis over 20–30 years, combining all of the relevant data in the literature and archives. Our more comprehensive approach lets us reconcile some of the discrepant conclusions reached previously. More importantly, we will introduce and demonstrate new analysis approaches to probe the circumnuclear torus properties in greater depth than has been possible previously.

In addition, all the dust reverberation mapping studies published so far only probe the very inner part of the torus at  $\lambda \sim 1\text{--}4 \mu\text{m}$ . We will report the first IR reverberation analysis of the dusty component of an AGN at  $\sim 10 \mu\text{m}$ , providing constraints on the warm dust component that dominates the IR energy output. In fact, NGC 4151 is likely the only object that allows this kind of study thanks to its significant UV/optical light variations and the  $\sim 30$ -year coverage of repeated  $\sim 10 \mu\text{m}$  observations. We will also report the lack of long-term variability of this AGN at 20–24  $\mu\text{m}$  and 34–37  $\mu\text{m}$ , providing insights into the outer regions of the infrared source when combined with the 10  $\mu\text{m}$  dust reverberation signals.

With a comprehensive analysis of the dust reverberation signals in the J, H, K, L and N bands and constraints on IR variability at 20–40  $\mu\text{m}$  over 20–30 years, this paper will: (1) give insights to the torus radial and vertical structures as a function of wavelength; (2) explore possible temporal evolution of the torus structures; and (3) provide tests of the observed dust reverberation signals against the predictions of current torus models. Integrating these results with observational constraints from other wavelengths/methods and physical insights obtained from previous theoretical studies, we can establish a complete picture of the dusty heart of NGC 4151 at diverse physical scales.

This paper is organized as follows. In Section 2, we describe the data collection and how the light curves have been constructed. Section 3 explores the physical origins of various features in the AGN IR light curves and retrieves the dust reverberation signals as a function of wavelength. We also explore the possible time-evolution of the AGN torus properties. In Section 4, by integrating our reverberation results with other observations, we provide constraints on the torus dust temperatures, vertical structures, and radial sizes as a function of observed wavelength and the possible dust grain properties. We also compare these results and popular torus models, specifically showing that the 10  $\mu\text{m}$  reverberation behavior is not as predicted by current clumpy torus ones. A final summary is provided in Section 5.

We adopt a distance of 15.8 Mpc to NGC 4151 (Yuan et al. 2020).

## 2. LIGHT CURVE CONSTRUCTION

### 2.1. Sources of Time-series Data

Optical photometry of NGC 4151 was taken from the literature and as available in VizieR, i.e. Lyuty and Doroshenko (1999); Doroshenko et al. (2001); Lyuty (2005); Sergeev

et al. (2005); Shapovalova et al. (2010); Roberts & Rumstaj (2012); Oknyansky et al. (2013)<sup>1</sup>; Koshida et al. (2014)<sup>2</sup>; Oknyansky et al. (2018); Shomshekova et al. (2019)<sup>3</sup>.

NGC 4151 was extensively monitored in the J, H, K, and L bands at the Crimean Observatory of the Sternberg Astronomical Institute (SAI) between 1994/05 and 2018/08; the measurements are available at <http://www.sai.msu.ru/basa/inf.html> and the observations are described in Lyuty et al. (1998); Shenavrin et al. (2011); Taranova & Shenavrin (2013); Oknyansky et al. (2018). NGC 4151 was monitored in the V- and K-bands between 2001/03 and 2007/07 in the Multicolor Active Galactic Nuclei Monitoring (MAGNUM) project (see Koshida et al. 2014, and references therein). We collected these data from Koshida et al. (2014). In addition, Schnülle et al. (2015) monitored the near-IR emission of NGC 4151 from 2010 January to June and from 2012 February to 2014 June. We collected this J, H, K band photometry from their paper. We also collected K-band photometry of NGC 4151 from 1975 to 1980 (Allen 1976; Stein & Weedman 1976; Kemp et al. 1977; O’Dell et al. 1978), Lebofsky & Rieke (1980) and Cutri et al. (1981).

To explore the variability behavior of NGC 4151 at  $\sim 10 \mu\text{m}$ , we collected observations from Rieke & Lebofsky (1981), Ward et al. (1987), Soifer et al. (2003), Radomski et al. (2003), Gorjian et al. (2004), Weedman et al. (2005) and Asmus et al. (2014) and the ISOPHOT-S spectrum (Sturm et al. 1999), the *Spitzer*/IRS spectrum, *AKARI*/IRC S9W photometry and *WISE* W3 photometry, and converted them into the same system, as detailed in Section 2.3. These data cover a length of 36 years from 1975 through 2010.

Besides the optical and IR data, NGC 4151 has also been intensively monitored in the hard X-ray (15–50 keV) by the *Swift*/Burst Alert Telescope (BAT). We collected its light curve from the *Swift*/BAT Hard X-ray Transient Monitor that covers the time period between 2005/02 and 2020/07 (Krimm et al. 2013). We combined all the measurements and smoothed the X-ray light curve with a 50-day window to improve the ratio of signal to noise. In addition, the flux from

<sup>1</sup> In some references, the author name “Oknyansky” has been transliterated as “Oknyanskij”. We have adopted “Oknyansky” throughout the main text of the paper but used “Oknyanskij” in the reference list when necessary so the citation can be readily found in the Astrophysics Data System (ADS).

<sup>2</sup> We transformed the V photometry in Koshida et al. (2014) to B, based on colors from the other programs.

<sup>3</sup> The errors on the nuclear B-band flux have been estimated by detrending (linearly) the dependence of B–V vs.  $0.5 \times (B+V)$ , evaluating the scatter after detrending, and then correcting for the galaxy flux within the measurement aperture from Doroshenko et al. (1998). These steps are important because (1) the true errors in measuring the galaxy are likely to be significantly larger than the nominal photometric internal errors, particularly in the face of atmospheric seeing and its variations from night to night (e.g., Peterson et al. 1995); and (2) although large measurement apertures significantly reduce the seeing issues, they also dilute the nuclear flux with that from the galaxy and the resulting net error in the nuclear flux needs to reflect this effect. The resulting errors (corrected to an aperture of  $6''$ ) range from  $\sim 5\%$  for the SAI photometry when the nucleus is bright to  $\sim 8\%$  for the photometry of Shomshekova et al. (2019). Given the amplitude of the variations in nuclear B-band output, these errors are not a significant issue in our analysis.

NGC 4151 has also been tracked by the Monitor of All-sky X-ray Image (MAXI) at 2–20 keV with the Gas Slit Camera (GSC) since 2009 August. With the MAXI on-demand process tool provided by the team<sup>4</sup>, we extracted the 2.0–6.0 and 6.0–20.0 keV light curves with a 30-day binned window to increase the signal to noise ratio. Finally, we have used the Band A, 1.3–3 keV, data from the Rossi X-ray Timing Explorer (RXTE) All-Sky Monitor (ASM) (Levine et al. 1996) to track the low-energy X-ray output. We co-added these data over  $\sim 3$  month time intervals to obtain sufficient signal to noise.

## 2.2. Subtraction of Host-galaxy Flux

Although it does not enter into our analysis of the variations, an accurate determination of the galaxy contribution is necessary to determine if there is a significant underlying non-variable excess flux above the stellar output. We will therefore subtract the galaxy contribution to put all the light curve data on the same scale.

We used B-band as a measure of the nuclear optical/UV luminosity, because it is relatively high contrast relative to the galaxy and has been measured frequently and accurately. We took the galaxy component in this band from Lyuty and Doroshenko (1999) and subtracted it from all of the SAI B-band photometry. Since we found from the K-band measurements that determining galaxy components directly from limited sets of measurements is challenging (as discussed below), we used a different approach for the rest of the measurements. We adjusted all the other photometry to match the SAI measurements in regions of overlap by converting the data to a consistent flux scale and then subtracting a constant term from the fluxes (without changing their normalization).

Estimates of the host galaxy K-band brightness in the literature differ substantially. We have therefore used the J-H vs. H color-magnitude diagram to obtain an independent estimate, with details provided in Appendix A. The behavior of NGC 4151 in J-H vs H is illustrated in Figure 1. The blue dots are the SAI photometry transformed to the 2MASS system (after rejecting four outliers). The line is the predicted behavior assuming a flux density at H of 89 mJy for the host galaxy and a ratio of flux densities for the excess variable component at H to J of 1.75. These constraints on both the galaxy flux density and the color of the excess are reasonably tight; they translate at  $K_S$  to  $73 \pm 5$  mJy in  $12''$  and  $59 \pm 4$  mJy in  $8''.3$  apertures, respectively. There are intervals where the flux at J above the galaxy contribution is only 4 mJy, or just  $5 \pm 6\%$ ; i.e., close to zero within the errors. Since the J-H color at minimum light matches expectations for a normal galaxy, the nuclear emission in the H band is also negligible at these times. However, H-K and K-L were much redder than standard galaxy colors even at minimum light; we used typical galaxy colors (see Appendix A) normalized to H to project the flux from the galaxy to K and L,

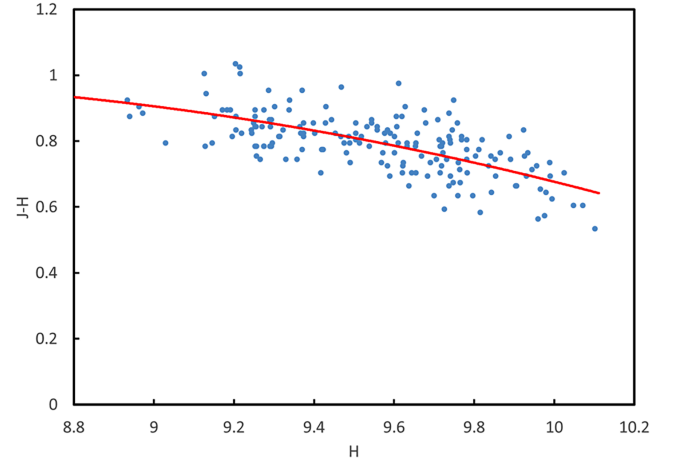


**Figure 1.**  $J - H$  vs  $H$  for the SAI photometry of NGC 4151. The blue dots are the measured values, and the red curve is the expected relation assuming that the variable component has a constant  $J - H$  of 1.12, i.e., a ratio of frequency-unit flux densities of 1.75, and the galaxy J and H magnitudes are 10.83 and 10.15, respectively, corresponding to  $74.5 \pm 5$  and  $89 \pm 6$  mJy, through a  $12''$  aperture.

and then subtracted the galaxy component from all the SAI measurements.

All the other infrared photometry sequences had significant time overlap with the SAI one. As at B-band, we converted magnitudes to fluxes and then subtracted a constant flux from all the measurements in a given photometry set (but with no adjustment to the flux scale), which we adjusted to force agreement for the times of overlap. For the Koshida et al. (2014) measurements, we needed to increase the subtracted value from their  $44 \pm 4$  to  $66$  mJy, consistent within the mutual errors with our value derived above.

We used the resulting generally smoothly varying light curve at K to search for spurious outliers. We found that the photometry from the SAI group seems unreliable on nights when results are reported for only a subset of the four bands; for example, many of these measurements are outliers from the K-band light curve, but also frequently report strange variations, e.g., by 0.3 magnitudes in one band while an adjacent band does not change significantly. We therefore retained only those data that had consistent behavior among the bands and with adjacent nights. We then combined these infrared measurements with those from Koshida et al. (2014) and Schnülle et al. (2015). The resulting very well sampled K-band light curve plus the accompanying less-well-sampled light curves in J, H, and L are the foundation for our analysis.

Besides these data, we also converted the K-band measurements of NGC 4151 in Allen (1976), Stein & Weedman (1976), Kemp et al. (1977), O’Dell et al. (1978), Lebofsky & Rieke (1980) and Cutri et al. (1981) into a consistent flux scale and built a single-band IR light curve covering  $\sim 1975$ –1980. This dataset provides a comparison to the  $10 \mu\text{m}$  measurements in 1975 and 1976.

<sup>4</sup> <http://maxi.riken.jp/mxondem/index.html>

Figure 2 shows the full B, J, H, K, L galaxy-subtracted light curves, which will be analyzed in Section 3. These data are provided in the online journal and a small portion is given in Table 1 to show its basic format.

**Table 1.** Galaxy-subtracted B, J, H, K, L light curves of NGC 4151

JD	Band	Flux (mJy)	Source
2439941.4	B	26.566	Lyuty et al. (1999)
2439941.4	B	24.387	Lyuty et al. (1999)
2439944.3	B	23.588	Lyuty et al. (1999)
2439945.3	B	22.161	Lyuty et al. (1999)
2439945.3	B	22.846	Lyuty et al. (1999)
...	...	...	...

NOTE—Table 1 is published in its entirety in the machine-readable format. A portion is shown here for guidance regarding its form and content.

### 2.3. Photometry at 10 $\mu\text{m}$

In the 36 years from 1975 through 2010, there are 28 measurements at  $\sim 10 \mu\text{m}$  useful for light curve tracking (excluding a few of low signal to noise, or with spectrometers with undetermined slit losses). Although these are unevenly spaced, with gaps of 5–10 years, they are adequate to test for lags on decadal timescales.

The different spectral bands and calibration approaches must be understood to construct an accurate light curve. A simple demonstration of real variations is, however, possible. The measurements of Ward et al. (1987) are with very similar photometric systems as those of Rieke (1978); Rieke & Lebofsky (1981) and there are enough sources in common with Rieke (1978) that the relative calibration can be determined directly. The five galaxies other than NGC 4151 with measurements in common show excellent agreement in the reported flux densities (average ratio of Rieke (1978) to Ward et al. (1987) values of  $0.964 \pm 0.065$ ), while the earlier (Rieke & Lebofsky 1981) measurements of NGC 4151 are higher than the later (Ward et al. 1987) ones by a factor of  $1.363 \pm 0.042$ . This estimate includes non-statistical errors as already within the Rieke & Lebofsky (1981) values, but at 7% additional for the Ward et al. (1987) ones. The two N-band measurements early in the 21st century (Gorjian et al. 2004; Radomski et al. 2003) are  $1.58 \pm 0.11$  times higher than the ones reported in Ward et al. (1987).

To generalize this result over the full baseline, we have assembled all the relevant measurements and corrected them to flux densities at  $10.6 \mu\text{m}$ , as summarized in Table 2. The reconciliation of the measurements to a common photometric basis is discussed in Appendix B.

### 2.4. Accretion disk variability traced in the X-ray

Czerny et al. (2003) compared the optical and X-ray light curves of NGC 4151 over several decades. They found

**Table 2.** NGC 4151 photometry transformed to  $10.6 \mu\text{m}$

JD	flux(mJy)	error(mJy)	Source
2442417	2058 <sup>1</sup>	124	Rieke & Lebofsky (1981)
2442433	2083 <sup>1</sup>	87	Rieke & Lebofsky (1981)
2442468	2021 <sup>1</sup>	112	Rieke & Lebofsky (1981)
2442494	2083 <sup>1</sup>	124	Rieke & Lebofsky (1981)
2442518	1897 <sup>1</sup>	112	Rieke & Lebofsky (1981)
2442466	2032	49	average of above five
2442808	2046 <sup>1</sup>	87	Rieke & Lebofsky (1981)
2442846	2046 <sup>1</sup>	112	Rieke & Lebofsky (1981)
2442869	2108 <sup>1</sup>	87	Rieke & Lebofsky (1981)
2442878	1922 <sup>1</sup>	62	Rieke & Lebofsky (1981)
2442888	1972 <sup>1</sup>	112	Rieke & Lebofsky (1981)
2442856	2002	38	average of above five
2445116	1116 <sup>1</sup>	168	Ward et al. (1987)
2445118	1401 <sup>1</sup>	189	Ward et al. (1987)
2445117	1259	90	average of above two
2445371	1724 <sup>1</sup>	149	Ward et al. (1987)
2445498	1440 <sup>2</sup>	290	IRAS
2445766	1275 <sup>1</sup>	109	Ward et al. (1987)
2450211	1370	140	Sturm et al. (1999)
$\sim 2450401^4$	1180 <sup>3</sup>	118	MSX
2451628	2340 <sup>5</sup>	230	Gorjian et al. (2004)
2451680	2440 <sup>6</sup>	244	Soifer et al. (2003)
2452037	2324 <sup>1</sup>	232	Radomski et al. (2003)
2453104	1900	133	Weedman et al. (2005)
$\sim 2454876^4$	1820 <sup>3</sup>	130	AKARI
2454990	1440 <sup>7</sup>	101	Asmus et al. (2014)
2454990	1300 <sup>7</sup>	91	Asmus et al. (2014)
2455285	1580 <sup>7</sup>	111	Asmus et al. (2014)
2455285	1470 <sup>7</sup>	95	Asmus et al. (2014)
2455320	1353 <sup>7</sup>	95	Asmus et al. (2014)
$\sim 2455321^4$	1507 <sup>3</sup>	150	WISE

<sup>1</sup> Corrected via bandpass correction computed using Spitzer IRS spectrum (Weedman et al. 2005)

<sup>2</sup> Average of values from Sembay et al. (1987); Sanders et al. (2003). Adjusted by 0.12 Jy for contribution of star formation in the host galaxy, based on fitting a template (Rieke et al. 2009) to the far infrared  $\lambda \geq 100 \mu\text{m}$  measurements. Corrected to  $10.6 \mu\text{m}$  using Spitzer/IRS spectrum (Weedman et al. 2005)

<sup>3</sup> Corrected to  $10.6 \mu\text{m}$  using Spitzer IRS spectrum (Weedman et al. 2005)

<sup>4</sup> When measurements over an extended mission are combined, a typical date is shown as being approximate.

<sup>5</sup> Reported value is corrected for flux outside central PSF by taking the average of the lower limit reported in Gorjian et al. (2004) and the correction derived by Radomski et al. (2003).

<sup>6</sup> Corrected for flux outside central PSF according to Radomski et al. (2003). Corrected to  $10.6 \mu\text{m}$  using Spitzer IRS spectrum (Weedman et al. 2005)

<sup>7</sup> Rereduced to use aperture photometry of  $\sim 4''$  diameter. Corrected to  $10.6 \mu\text{m}$  using Spitzer IRS spectrum (Weedman et al. 2005)

an independent long-timescale (over  $\sim 10$  years) component that dominates the optical variations, but that the optical variations also contain a short-timescale component well-correlated with the X-ray ones over 5-1000 days. Edelson et al. (2017) also confirmed the strong correlation between



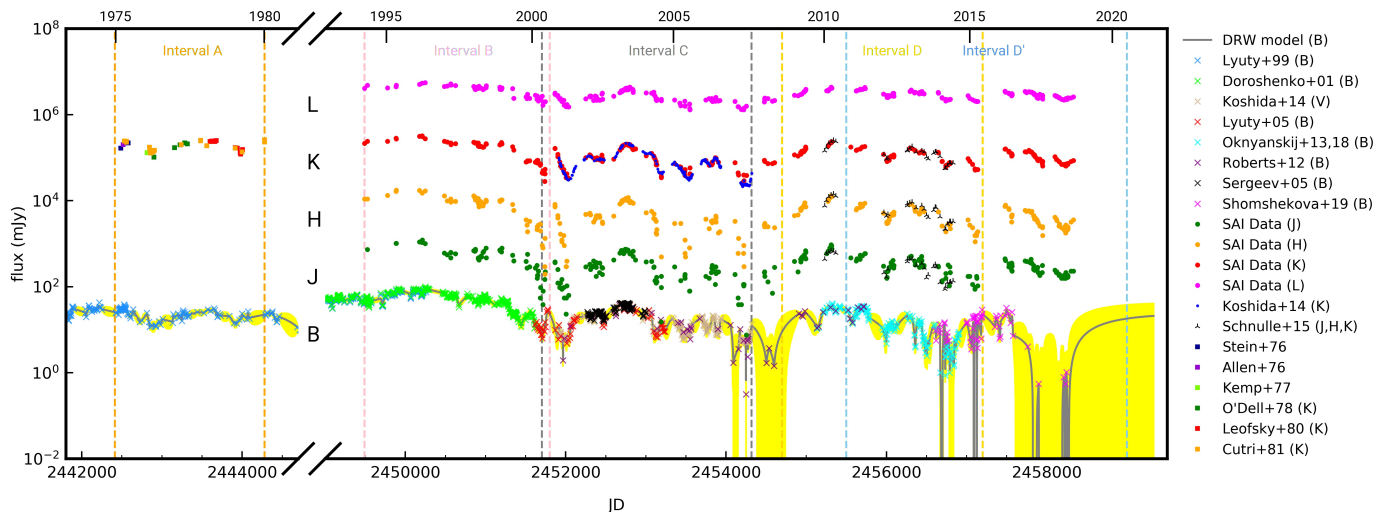


**Figure 2.** The B, J, H, K, L light curves of NGC 4151. The sources for and adjustments to individual light curves are discussed in the text. We also show a damped-random-walk (DRW) model (JAVELIN; Zu et al. 2013) to interpolate this light curve (the line). We have arbitrarily scaled J, H, K, L light curves by factors of 10, 100, 1000, 10000 to separate them for clarity. The time periods of Interval A, B, C, D, D’ (see Section 3.1) are indicated with vertical lines in different colors.

the UV/optical and X-ray variability of NGC 4151, although they also found that the UV/optical band variation lags 3–4 days behind the hard X-rays. Since the IR lag of NGC 4151 is less than 100 days, we have used the short-time X-ray variability to pin down the IR lag measurements when the optical data are limited. This approach is successfully illustrated by Noda et al. 2020. It is particularly useful for JD 2457000–2458500, when the optical data are too poor for our reverberation analysis.<sup>5</sup> To make a consistent comparison, we generate a synthetic B-band light curve by scaling and shifting the X-ray light curve and adding a 4-day delay (as found by Edelson et al. (2017)).

### 3. DUST REVERBERATION ANALYSIS

In Section 3.1, we provide an initial evaluation of the optical and IR J, H, K, L light curves and point out several issues that have been overlooked by the previous dust reverberation analysis. Section 3.2 introduces our analysis methods and establishes that there are two main time lags that contribute to the AGN reverberation signals at 1–4  $\mu\text{m}$ . Section 3.3 discusses the evolution of hot dust reverberation signals over 30-years. We compare these results with previous near-IR reverberation studies of NGC 4151 in Section 3.4. Finally, we report the detection of a IR time lag from the AGN warm dust emission ( $\sim 300\text{K}$ ) in the N-band and the lack of IR variations of NGC 4151 at wavelengths at 20–40  $\mu\text{m}$  in Section 3.5.

#### 3.1. JHKL Reverberation Signals and Challenges for Simple Optical-IR Cross-correlation Analysis

<sup>5</sup> Although supernova 2018aoq was discovered on 2018-04-01 (JD:2458208), 73’’ from the NGC 4151 nucleus (see <http://www.rochesterastro.org/sn2018/sn2018aoq.html>), we do not see its influences in the X-ray light curves, possibly due to it being relatively faint compared to the AGN.

Since our light curves come from various sources with different cadences, we separate the time epochs into four intervals as shown in Figure 2, with Interval A from JD 2442414 through 2444281 (January, 1975 through February 1980), prior to our multi-band IR reverberation analysis; Interval B from JD 2449490 through 2451800 (May, 1994 through September 2000); Interval C from JD 2451704 through 2454319 (June, 2000 through August, 2007); and Interval D from JD 2454700 through 2457200 (August, 2008 through June, 2015). In addition, we denote the time period covered by *Swift* observations as Interval D’, which spans JD from 2455500 through 2459000 (November, 2010 through May, 2020).

##### 3.1.1. General variability behavior and time sampling

Reverberation mapping has been applied extensively in the ultraviolet, optical, and for emission lines. The requirements for success include a measurement sequence that fully samples the variations (e.g., Nyquist sampling) and to carry out this sequence for at least three times the longest reverberation lag, with modest gaps in longer datasets not strongly affecting the results (e.g., Horne et al. 2004). Below we will find lags of the infrared behind the blue signals of  $\sim 35$  and  $\sim 90$  days for NGC 4151. JHKL photometry is available from 1994 to 2018, but in general in intervals with significant gaps that may in some cases be inconsistent with these goals.

We initially focus on Interval C where we combine campaigns by the SAI and MAGNUM groups to improve the sampling at K. During this period there were also many campaigns at B-band, providing a very well sampled light curve. We compare the B and K-band light curves in Figure 3 during this interval, from JD 2451704 through 2454319 (June 8, 2000 through August 6, 2007), showing the very thorough data available in both bands. In favorable cases, the data extends over 5–6 periods of the shorter ( $\sim 35$  day) lag. There

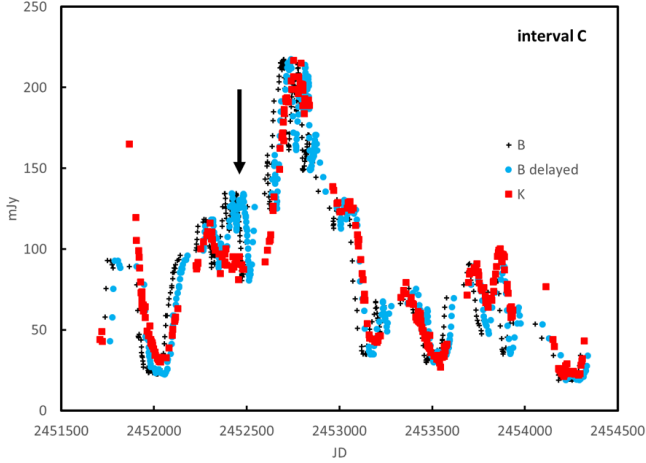


**Figure 3.** Light curves in Interval C at B (blue circles) and K (red squares) (the former delayed by 35 days and smoothed by taking a seven-point running average). The undelayed B-band data is indicated by + symbols and clearly leads the K-band behavior. Overall, the two sets of data are in very good agreement suggesting a reverberation delay of order 35 days. However, there is a significant discrepancy in the range indicated by the arrow.

is data for about six times the longer ( $\sim 90$  day) lag with an average sampling of about four times Nyquist and just two gaps, each of roughly one period.

The behavior during this period is largely consistent with the assumption that the K-band flux results from a reverberation of the nuclear signal (characterized by B-band) when it heats dust in the circumnuclear torus (but see next section). As a demonstration, in the figure we have smoothed the B-band data to reflect the light travel times for different zones of the torus and delayed it by 35 days (similar to that found by Oknyansky et al. (2018) of  $37 \pm 3$  days and consistent with our results reported below). This general agreement is consistent with most other previous work.

In Figure 4, we show the B-band and K-band light curves for Intervals B and D. For Interval B, there are nominally sufficient K-band observations for Nyquist sampling but their spacing results in the curve being significantly undersampled. For Interval D, there is an on-off pattern of roughly 180 days and generally poorer sampling than in Interval C.

### 3.1.2. Uncorrelated Variations Between the Optical and IR

Previous studies have assumed that the reverberations strongly dominate the relationship between the optical and near infrared. However, this is not always correct. As indicated with an arrow in Figure 3, there was an outburst in the B-band that did not reach the torus, since the IR emission seems to have little reaction. Figure 5 shows an expanded view of this event. The B-band flare is verified by three independent measurement series and the lack of a corresponding K-band feature by two independent measurement series.

Such behavior shows that, on top of the expected reverberation behavior, there could be outbursts from the central source/accretion disk (e.g., jets) that are directed away from

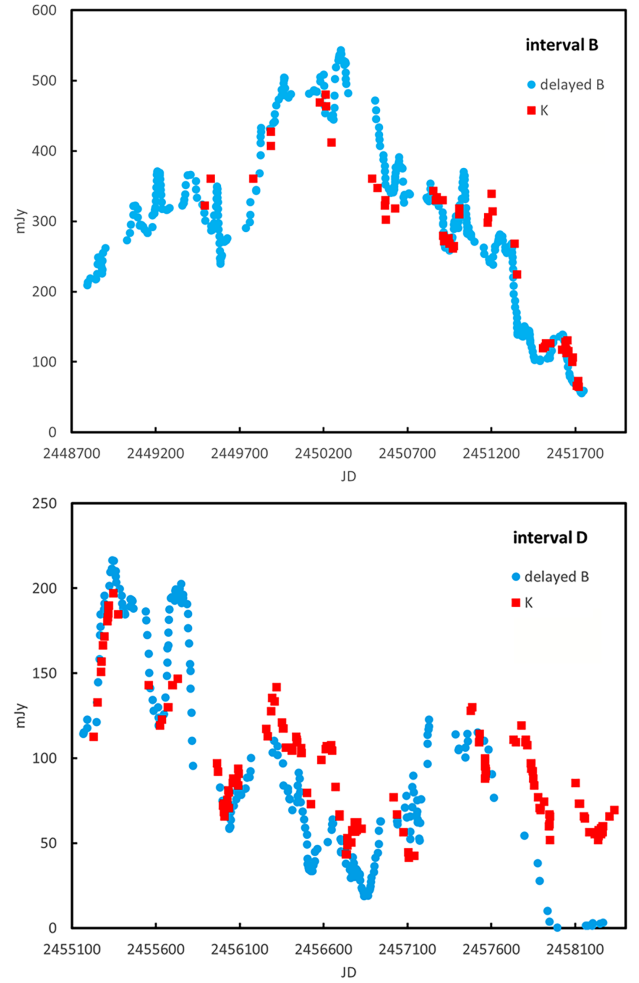


**Figure 4.** Light curves for B-band and K-band in intervals B and D. To provide a rough match to the B-band curve, the K-band fluxes have been multiplied by 1.5 in interval B and by 0.81 in interval D.

the torus or other events confused with central activity that do not reach the circumnuclear torus (e.g., nearby supernovae: the B-band data are taken through an aperture of  $\sim 2$  kpc diameter at the galaxy). Figure 6 shows a similar event in the IR light curve of another type-1 AGN, MCG 08-11-011 (the data are from Koshida et al. 2014), indicating such behavior might be common. The various possibilities – supernova, tidal disruption event and beamed jet variability – all can produce variable signals on a timescale of  $\sim 100$ – $300$  days.

For Interval D, there is a different behavior, namely a dramatic drop in the B-band curve beyond JD 2457900 that is not reflected at K-band.

That the B-band curve is influenced by phenomena not reflected in the K-band adds uncertainty to conventional reverberation analyses between the optical and IR. To circumvent these issues, in our analysis described in Section 3.2 we will start with interval C both because of its much better sampling in the infrared and because the B-band and K-band seem to track each other much better than in interval D. To avoid

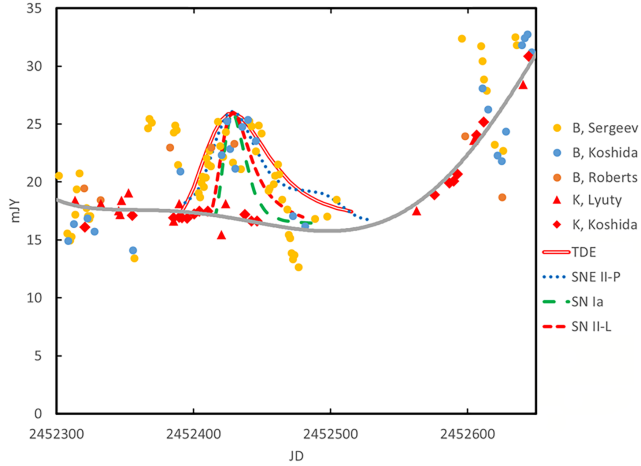


**Figure 5.** Expanded view of the 35-day-delayed B and the K band light curves. The solid gray line is a polynomial fit to the K-band data. The peak in B-band near JD 2452430 is apparent in three independent sets of measurements, while the lack of this peak is shown by two independent sets of K-band ones. We show four possible light curves, for a SNE Ia, SNE II-L, SNE II-P (Wheeler 1990) or a tidal destruction event (TDE), although known TDEs are more luminous (van Velzen et al. 2020).

completely any uncorrelated B-band variations, we will first compare the J-, H-, and L-band curves with the K-band one. We then compare the well-sampled K-band curve with the B-band one. In this latter analysis, we mask the IR-uncorrelated flare in B-band. This approach gives us a robust lag of all three IR bands relative to each other and to the B-band. We will then carry out additional analyses, e.g., for interval D, to demonstrate that their behavior is consistent within the significantly larger uncertainties.

### 3.1.3. Evidence for Multiple Dust Components

Before progressing to reverberation modeling, we compute the standard deviations of the light curves as an unbiased measure of the wavelength dependence of the IR variability. This approach should give a good approximation for the SED of the dust components most directly heated by the AGN. The results are presented in Figure 7. They are reasonably matched by the Elvis normal AGN template, as is consistent with our SED decomposition of NGC 4151 based on high spatial-resolution data in Lyu & Rieke (2018).

After subtracting the accretion disk variability in the infrared bands derived from B band with a  $\Delta f_\nu \propto \nu$  dependence (see Section 3.2.2), we fitted the near- to mid-IR dust-only variability SED with black-body models. Such models should be applicable for wavelengths short of  $\sim 4 \mu\text{m}$ ; the longer wavelength behavior is not constrained. As demonstrated in Figure 7, we needed two, instead of one, black body components to match the observations: one with a dust tem-

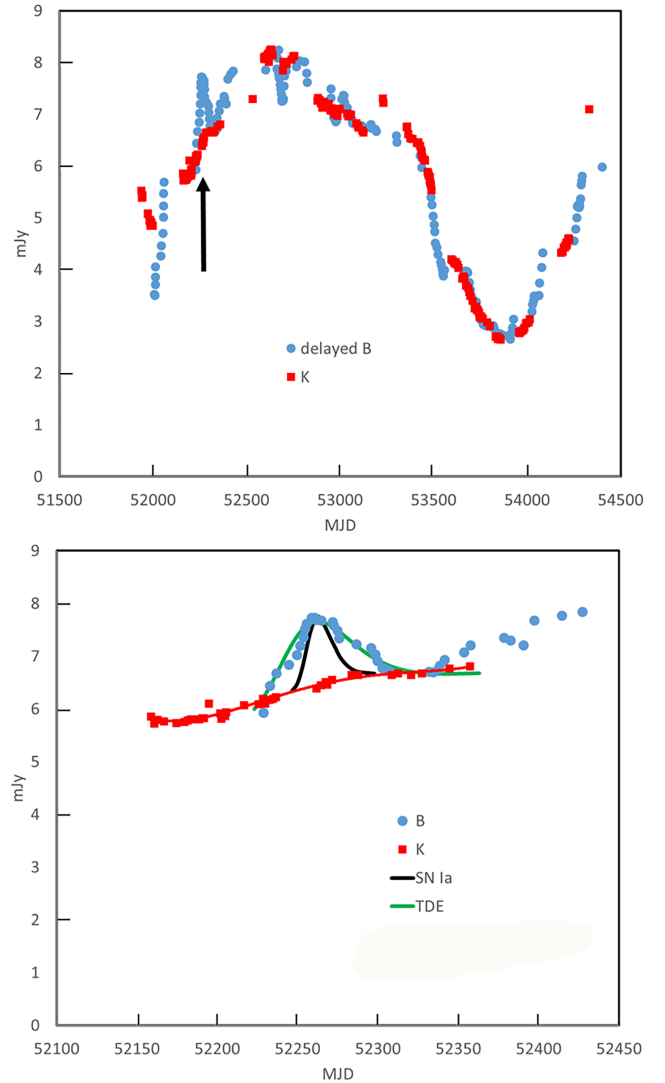


**Figure 6.** A similar event to that in Figure 5, but in comparing the V-band and K-band light curves of MCG 8-11-011, from Koshida et al. (2014). Again, the behavior of the event is similar to that of a SNE II-P or a TDE.

perature of  $\sim 1600\text{--}2500 \text{ K}$ <sup>6</sup> (“Component A”) and another with a dust temperature of  $\sim 1000 \text{ K}$  (“Component B”).

We use a double black-body to investigate the time-dependent behavior of the SED as summarized in Figure 8. The dust temperatures of the two components are reasonably stable<sup>7</sup> while their emission strengths correlate with the B-band light curve. This confirms that two dust components

<sup>6</sup> Due to the lack of constraints at shorter wavelengths and the strong contamination from the accretion disk variability, the temperature of this component cannot be accurately determined. We adopt an upper value of 2200 K.

<sup>7</sup> Small variations similar to those found by Schnülle et al. (2015) are not ruled out by this simple analysis.

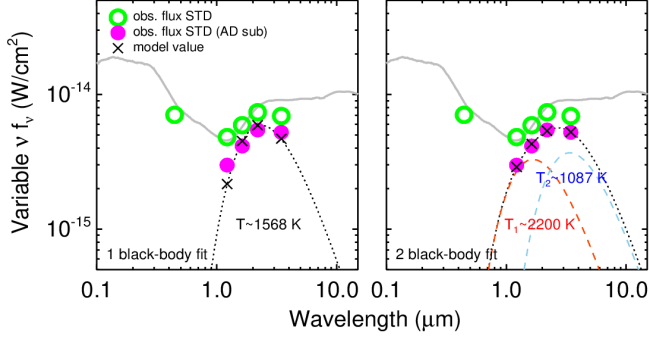


**Figure 7.** Variability SED of NGC 4151. We show the standard deviations of the B, J, H, K, L light curves as green open circles. After subtracting the accretion disk variability contamination, the infrared dust SED (purple dots) is fitted with one single black body (left panel) and two black bodies (right panel). The model SEDs, shown as black crosses, only fit the observations for the two black body model. For comparison, we show the Elvis-like AGN normal template as grey lines.

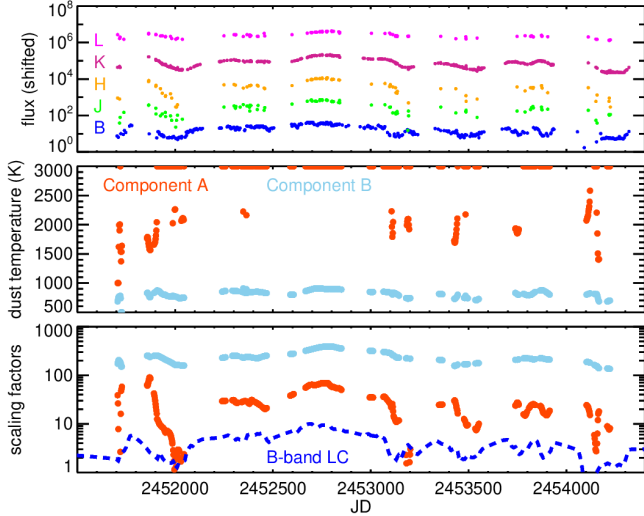


**Figure 8.** NGC 4151 light curves and the time dependence of the double-black-body best-fit parameters in Interval C.

with different temperatures are likely to be responsible for the variable  $\sim 1\text{--}4\ \mu\text{m}$  emission.

The presence of two dust components with different temperatures is not a surprise. Carbon and silicates are the dominant species of interstellar grains, and presumably also for the grains in the AGN torus. The sublimation temperatures,  $T_{\text{sub}}$ , of these grains are 1500–1800 K for graphite and 800–1000 K for silicates; consequently only graphite grains would survive at the innermost regions and silicate grains would be distributed to larger radii. Assuming an optically-thin environment, the sublimation radius,  $R_{\text{sub}}$ , for graphite grains is

$$\frac{R_{\text{sub,C}}}{\text{pc}} = 1.3 \left( \frac{L_{\text{UV}}}{10^{46} \text{erg s}^{-1}} \right)^{0.5} \left( \frac{T_{\text{sub,C}}}{1500\text{K}} \right)^{-2.8} \left( \frac{a_{\text{C}}}{0.05\ \mu\text{m}} \right)^{-0.5}, \quad (1)$$

based on the relation in Barvainis (1987) with a  $a^{-1/2}$  term

to approximate the dependence on the grain size  $a$  (Kishimoto et al. 2007). Here  $L_{\text{UV}}$  is the UV luminosity in the direction of the grains. Similarly for silicate dust grains, adopting the absorption efficiency of astronomical silicate (Draine & Lee 1984; Laor & Draine 1993), we have

$$\frac{R_{\text{sub,S}}}{\text{pc}} = 2.7 \left( \frac{L_{\text{UV}}}{10^{46} \text{erg s}^{-1}} \right)^{0.5} \left( \frac{T_{\text{sub,S}}}{1000\text{K}} \right)^{-2.8} \left( \frac{a_{\text{S}}}{0.05\ \mu\text{m}} \right)^{-0.5}. \quad (2)$$

Thus the two temperatures inferred from our variability analysis imply that the inner structure of the dust torus is governed by grain sublimation (e.g., Rieke & Lebofsky 1981; Barvainis 1987) and thus might have two characteristic radii. We will test this hypothesis by seeing if the reverberation signals show two distinct lags in the IR light curves.

### 3.2. Near-IR Reverberation by Two Dust Components

#### 3.2.1. Subtraction of Accretion Disk Variability in the IR

To study the dust reverberation signals of NGC 4151, we need to remove the IR variations of the accretion disk itself from the IR light curve. The infrared continuum from the accretion disk is not well-determined. Although theoretically it might be expected to go as  $\nu^{1/3}$ , it has been difficult to confirm such behavior in the optical (Gaskell 2008) and thus there is no obvious reason to adopt it in the infrared. One approach is to do profile fitting to remove the contribution of the galaxy and deduce a nuclear spectrum (e.g., García-Berete et al. 2019). However, we found in Section 2.2 surprisingly large discrepancies in such analyses. Therefore, we used the variability to constrain the nuclear spectrum, using the observations of Schnülle et al. (2015). We assumed that the  $z$  band ( $0.9\ \mu\text{m}$ ) is dominated by the accretion disk and the K band by the thermal reradiation and then adjusted the mixture of signals from each to match the variations of the J and H bands. The preferred mixture is determined by ratioing to the true J and H band fluxes and minimizing the standard deviation of these ratios over all 29 epochs. This analysis indicates that the SED falls more rapidly than  $\nu^{1/3}$ , although it does not have sufficient wavelength baseline to derive a full IR spectrum independently.

We also used the wavelength dependence of the variability amplitude of NGC 4151 from the  $\sim 10$  years of BVRI photometric observations by Roberts & Rumstay (2012); these data cover a similar time period to Interval C, where our analysis is focused. We smooth each light curve with a window of three data points and then take the variation amplitude as the difference between the max and min flux values. We find  $\Delta f_{\text{B}} : \Delta f_{\text{V}} : \Delta f_{\text{R}} : \Delta f_{\text{I}} = 1.88 : 1.66 : 1.22 : 1$ , which can be described as  $\Delta f_{\nu} \propto \nu$ . Since there is no obvious physical reason for a turn-over of the  $\Delta f_{\nu}$  slope just entering the near IR, we adopted the same  $\Delta f_{\nu} \propto \nu$  through the near-IR, i.e.

$$F(t)_{\text{IR, dust}} = F(t)_{\text{IR}} - F(t)_{\text{OPT}} \left( \frac{\nu_{\text{IR}}}{\nu_{\text{OPT}}} \right)^{1.0} \quad (3)$$

where  $F(t)_{\text{IR}}$  is the observed light curve. Because the spectrum of the infrared excess rises steeply through  $2\ \mu\text{m}$  (in



Section 2.2, we showed the excess has an equivalent power law index  $< -2$ ), the possible range in the nonthermal SED we subtract should have little effect on our results. To confirm this, we repeated our analysis assuming a  $\nu^{1/3}$  nonthermal spectrum, finding no significant change.

### 3.2.2. Basic Dust Reverberation Fitting Method

Our lag analysis is a two-step progress, as introduced in Lyu et al. (2019): we first interpolate the driving light curve (usually in the optical) with a damped random walk (DRW) model and smooth it when necessary, and then this light curve model is shifted along the time axis and scaled along the amplitude axis to match the driven light curve (usually in the IR). Besides quantifying the time lag between the IR and optical variability, we can constrain their relative variation amplitudes. For two lags, the reverberation signal is

$$F(t)_{\text{IR, dust}} = \text{AMP}_1 \times \langle F(t - \Delta t_1)_{\text{OPT}} \rangle + \text{AMP}_2 \times \langle F(t - \Delta t_2)_{\text{OPT}} \rangle + F_{\text{const.}} \quad (4)$$

The first two terms on the right of the equation represent two reverberation signals;  $\text{AMP}_1$ ,  $\text{AMP}_2$  are the ratios between the optical light curve and the corresponding IR reverberation flux amplitude, and  $\langle F(t - \Delta t_1)_{\text{OPT}} \rangle$ ,  $\langle F(t - \Delta t_2)_{\text{OPT}} \rangle$  denote the smoothed optical light curve model with different time lags. The third term  $F_{\text{const.}}$  is the sum of all non-variable components. A single lag is described by setting  $\text{AMP}_2 = 0$ .

There are a number of approaches to evaluating the lag between the light curves. In Lyu et al. (2019), we used a high degree of smoothing of the driving light curve to retrieve the dust reverberation signals. Despite sampling with WISE data generally well below the Nyquist rate, we obtained consistent time lag measurements compared with the classical cross-correlation analysis and with the expectation that the lags would scale with the square root of the AGN luminosity. In this approach, a  $\chi^2$  minimization can be used (see Appendix C2 in Lyu et al. 2019). However, we have much better sampling for the near-infrared bands (JHKL) in NGC 4151 and can go beyond the high degree of smoothing we used previously (and in this paper at N-band). We smooth only very modestly with the DRW technique to fill in gaps, leaving the potential lag times intact. To find the best-fit parameters and their uncertainties for these data, we use the Dynamic Nested Sampling package, *Dynesty*, to estimate the fitting parameters and Bayesian posteriors (Speagle 2020). Compared with other methods such as Markov chain Monte Carlo or the Levenberg-Marquardt technique, the fitting of *Dynesty* does not require any initial guess of the parameter values and can detect model degeneracies in the parameter space efficiently. As the maximum a posteriori (MAP) values of the parameters provide the maximum conditional probability of matching the observed data given a model weighted by a prior, we mainly quote such parameters as the “best fit” to the data. To describe the parameter uncertainties, the 1-D marginalized posteriors, i.e., the median parameter value with  $2\text{-}\sigma$  “uncertainties” (i.e., 2.5%, 50% and 97.5% quantiles), are also

used when necessary. To check the validity of these results independently, we have also used the interpolated cross correlation function (ICCF) method recommended by Peterson et al. (1998) and the improved ICCF ( $\text{I}^2\text{CCF}$  of Guo et al. (2021, in prep.) for the cross-correlation analysis between the IR light curves.

In Section 3.2.3, we first use a one-lag model to determine the lags of the infrared J, H, and L bands relative to the K-band, confirming the existence of a secondary dust time lag at the longer wavelengths (as previewed in Section 3.1.2). Next, in Section 3.2.4 we apply a two-lag analysis between the optical and IR light curves and put constraints on the time lags, dust temperatures and variability amplitudes of the IR reverberation signals from the two dust components.

### 3.2.3. Correlation Analysis between IR Bands

Since the K-band light curve in Interval C has relatively high cadence, we use it as the base curve to correlate against other IR light curves. To do so, we first subtracted the accretion disk contamination in all the IR light curves, following the description in Section 3.2.1. We then interpolated the K-band dust emission light curve with the DRM model to bridge gaps. We finally carried out one-lag dust reverberation mapping against the J, H, and L bands with *Dynesty*. As shown in Table 2 (further details in Appendix C), the J and H light curves are strongly correlated with the K-band light curve with lags close to zero. These results indicate that the reverberation signals in these three bands are dominated by the same dust component. This result is not surprising since all three bands fall close to the expected SED for carbon dust at its sublimation temperature.

As the L-band observes a longer wavelength, its variability signal can be a mixture of dust components with different temperatures (thus at different radii), as indicated by the variability SED fitting in Section 3.1.3. Adopting a temperature of  $\sim 1800$  K for the hot dust that is probed at J and H (consistent with the flux ratio derived in Section 2.2), its flux levels in  $f_\nu$  in the K and L bands are similar. To bring out any additional lag component, we subtract the K-band light curve from the L-band one, so that the signal from any other dust component will be more prominent in the L-band residual signal. After this subtraction, the remaining L-band signal is half due to the persistent (non-varying) component and half (peak-to-peak) due to the variable one. We correlate the K-band light curve with the L-band one after this subtraction; the results are provided in Table 3 (with details in Appendix C). The K-subtracted L band has an indicated delay of about 53 days relative to K. As shown in the next section, this lag difference is also consistent with the two-lag dust reverberation analysis between the optical and IR light curves.

The cadence in Interval B is inadequate to repeat this analysis. However, we have carried out a similar analysis for data in Interval D, where we improved the K-band cadence by combining the SAI light curve and the data from Schnülle et al. (2015). The results can be seen in Appendix C. Similarly to Interval C, the J and H bands are strongly correlated with the K-band with negligible lags ( $\sim -10$  days for

J,  $\sim -1.7$  days for H). In contrast, the L-band residual signal lags behind the K-band variability by  $\sim 34$  days, consistent with the result for Interval C within the larger uncertainties due to the lower cadence compared to Interval C. Interestingly, [Schnülle et al. \(2015\)](#) fitted two black bodies to their z, J, H, K light curves and derived dust lags at  $\sim 29$  and  $\sim 67$  days with a relative lag about 38 days in agreement with our result, but they rejected this fit.

We applied two additional independent approaches to test the *Dynesty* result of a lag of  $\sim 50$  days of L relative to K. [Peterson et al. \(1998\)](#) discuss issues with the standard cross correlation function (CCF) analysis both in accurate lag determination and in error estimation. We used their recommended model-independent Monte Carlo methods to overcome these issues. We carried out an interpolated cross-correlation function (ICCF) analysis with the PyCCF code ([Peterson et al. 1998](#); [Sun et al. 2018](#)) on the K-band (with the accretion disk variability removed) and L-band (with the accretion disk variability and the first lag signals, i.e. K-band, removed) light curves. Our approach follows closely the recommendations of [Peterson et al. \(1998\)](#). Adopting the flux randomization technique, we made 5000 Monte Carlo simulations to determine the cross-correlation centroid distribution (CCCD) and the cross-correlation peak distribution (CCPD) as well as the corresponding uncertainties. The results are shown in Figure 9. The centroid and peak lags for L-band behind K-band are  $48.97^{+13.90}_{-15.59}$  and  $51.0^{+17.0}_{-20.97}$  days for Interval C, respectively for CCCD and CCPD. They are  $35.14^{+16.82}_{-24.30}$  and  $34.00^{+16.86}_{-26.63}$  days for Interval D, i.e., consistent within the errors (the quoted uncertainties indicate where 15.87% of the trials fall above and below the indicated lags, respectively, i.e.,  $\sim 1 \sigma$ ). Both results agree well with the *Dynesty* analysis.

For another test, we used an Improved ICCF ( $I^2CCF$ ) tool ([Guo et al. 2021, in prep](#))<sup>8</sup>. The basic methodology of this code has been introduced in [Uttley et al. \(2003\)](#); [Arévalo et al. \(2008\)](#); [Chatterjee et al. \(2008\)](#) and [Max-Moerbeck et al. \(2014\)](#). Briefly speaking,  $\sim 10^3$  realizations of Monte Carlo simulations were made to produce optical and IR light curves with the DRW models. The simulated light curves are segments randomly selected from the DRM model predictions after a 100-times longer time coverage with the same observational constraints. The same cadence and uncertainties as the observations are then assigned to each simulated light curve (i.e., we independently evolve the optical and IR light curves and check their behavior over a long time period with the same observational conditions.) The CCFs of all the simulated light curves are then measured. The number of positive lags with the peak CCF value  $r_{\max}$  higher than the observed  $r_{\max}$  relative to the number of total simulations yields a  $p$ -value that describes the probability that a correlation signal between the two light curves could occur by chance. For the L-band data in the Interval C, we got a value of  $59^{+11}_{-19}$  days for the lag of L behind K. The  $p$ -value is 0.019, i.e.,

the null hypothesis that this lag detection (i.e., no lag) arises from noise can be rejected at the 98.1% ( $=1-p$ ) confidence level. This third method therefore is also in good agreement with the  $\sim 50$  day lag of L relative to K found previously.

In summary, we confirm that there are two dominant lag times in the JHKL data, consistent with the separate dust components as predicted in Section 3.1.3.

### 3.2.4. Reverberation Analysis of the Optical and IR Light Curves

To obtain further constraints on the torus structure, we now apply a two-lag dust reverberation model as described in Section 3.2.2 to the optical and IR light curves of NGC 4151 together. First, we fitted the B-band and individual IR light curves in pairs in Interval C, where the K-band light curve is best-sampled (details provided in Appendix C). Two components have been robustly detected with IR-to-optical lag values of  $\sim 40$  days and  $\sim 90$  days. The lag difference is consistent with the analysis of the K- and L-band light curves in the previous section. In addition, the relative strength of the long-lag component to the short-lag component increases as a function of wavelength, consistent with the SED fitting analysis in Section 3.1.3.

Besides fitting each IR light curve individually, we also combined all the IR light curves in Interval C and fitted them with an integrated model that includes two variable black body spectra with separated time lags and that fits all four infrared bands simultaneously. For this model, the dust emission at a particular IR wavelength  $F(t, \lambda)_{\text{IR,dust}}$  is related to the AGN optical light curve  $F(t, \lambda)_{\text{OPT}}$  by

$$F(t, \lambda)_{\text{IR,dust}} = F(t - \Delta t_1)_{\text{OPT}} \times B(T_1, \lambda) \times \text{AMP}_1 + F(t - \Delta t_2)_{\text{OPT}} \times B(T_2, \lambda) \times \text{AMP}_2 + F_{\text{const}}(\lambda), \quad (5)$$

where  $B(T_1, \lambda)$ ,  $B(T_2, \lambda)$  are the two black body spectra with different dust temperatures  $T_1$  and  $T_2$ ;  $\text{AMP}_1$ , and  $\text{AMP}_2$  are the corresponding time- and wavelength-independent scaling factors and  $\Delta t_1$ ,  $\Delta t_2$  are the time lags. Although the emission spectrum is likely to be more complex than just the two blackbodies included, the analysis in Section 3.1.3 shows that such an approximation provides a good fit and probably reflects first-order reality.

We used *Dynesty* to sample the model parameter space, deriving the best-fit model in Figure 10, and we summarize the best-fit parameters of this model in Table 4<sup>9</sup>. Figure 11 provides marginalized posterior probability distribution of the fitting parameters, showing that the model is well-constrained. The reported time lags are  $\Delta t_1 = 39.3^{+0.3}_{-0.2}$  days and  $\Delta t_2 = 86.3^{+1.7}_{-1.9}$  days, consistent with the cross-correlation analysis and the individual IR light curve fitting. The best-fit temperatures are  $T_1 = 2177^{+27}_{-25}$  K and

<sup>9</sup> We arbitrarily increased the fitting weights of the J, H, and K data at JD 2452700–2452900 by a factor of five to mitigate the fitting bias of the AMP parameter due to the relatively short duration and resulting modest sampling of the high-flux epochs. This adjustment did not significantly change the best-fit values of other parameters.

<sup>8</sup> <https://github.com/legolason/PyIICCF/>

**Table 3.** 1-lag best-fit parameter values of the J, H, L against K band light curves

Band	$\Delta t$		$\log(\text{AMP})$		$F_{\text{const}}$	
	Median <sup>1</sup>	MAP	Median	MAP	Median	MAP
Interval C: 2000/06–2007/05						
J(K)	$-0.70^{+0.63}_{-1.01}$	-0.55	$0.25^{+0.01}_{-0.01}$	0.25	$-8.49^{+0.29}_{-0.30}$	-8.45
H(K)	$2.44^{+0.14}_{-0.21}$	2.45	$0.35^{+0.01}_{-0.01}$	0.36	$-10.33^{+0.44}_{-0.40}$	-10.31
L(K)	$52.78^{+14.56}_{-26.14}$	53.55	$0.50^{+0.09}_{-0.08}$	0.52	$97.96^{+8.97}_{-8.68}$	97.10
Interval D: 2008/08–2016/01						
J(K)	$-9.84^{+3.71}_{-4.76}$	-9.38	$0.35^{+0.02}_{-0.02}$	0.35	$-14.01^{+0.91}_{-0.86}$	-13.96
H(K)	$-2.47^{+2.00}_{-3.49}$	-1.67	$0.56^{+0.03}_{-0.03}$	0.56	$-18.22^{+1.88}_{-1.82}$	-18.24
L(K)	$31.94^{+75.97}_{-37.12}$	34.11	$0.35^{+0.14}_{-0.12}$	0.36	$132.34^{+15.01}_{-19.45}$	131.09

<sup>1</sup>The “uncertainties” of these median values are  $2\sigma$  (i.e., 2.5%, 50% and 97.5% quantiles).

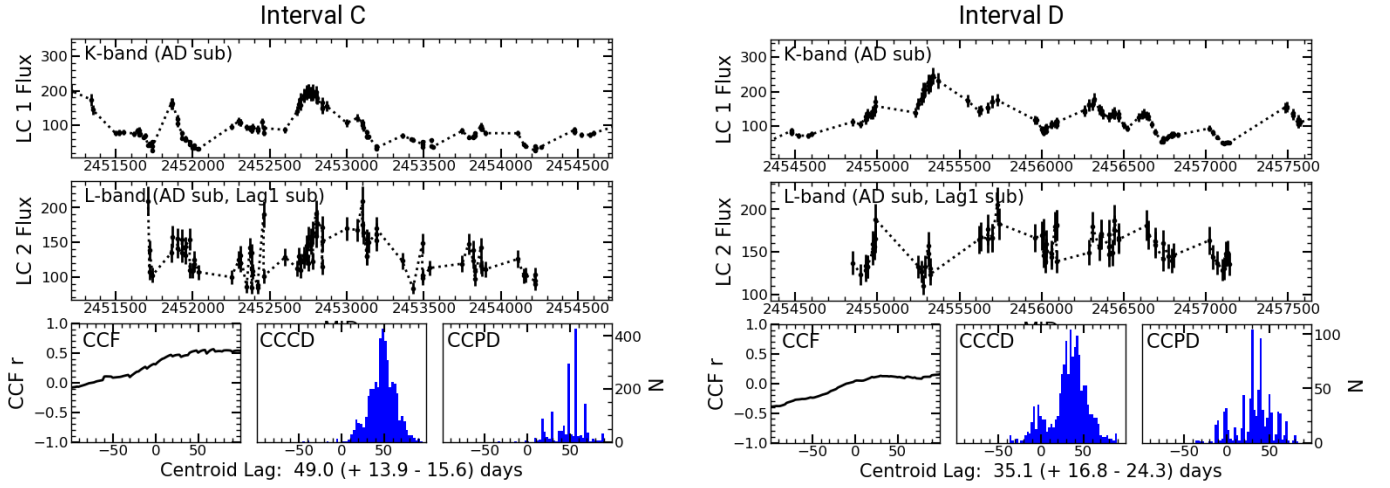


**Figure 9.** Interpolated cross-correlation analysis of the secondary lag in the L-band for Interval C (left) Interval D (right). The top and middle panels show the K-band light curve and the K-subtracted L-band light curve after removing the accretion disk (AD) variability, which have been used as input for the PyCCF code. The bottom three panels show the cross-correlation function (CCF), the cross-correlation centroid distribution (CCCD) and the cross-correlation peak distribution (CCPD). The breadth of the CCF indicates that there are additional components besides the variable one; for example, half of the signal in Interval C comes from a persistent component discussed later in the paper. The quoted centroid lags are for the CCCD cases; see text for further details. The secondary peak at zero lag in Interval D indicates that our simple subtraction of the K-band light curve from the L-band one left a residual signal with similar behavior to that at K-band.

$T_2 = 914^{+22}_{-20}$  K, also in good agreement with the variability SED analysis in Section 3.1.3.

Despite the poorer time sampling, we have applied the two-lag B-band and JHKL dust reverberation mapping model to the individual IR light curves in intervals A, B, D and D’ and summarize the best-fit parameters in Table 5. In all cases, the shorter lag is similar to that found for interval C, ranging from 30–40 days. The second lags for the intervals other than C have a wide scatter, presumably because of the various shortcomings in the data such as poorer time sampling and features in B-band that are not reflected in the IR, such as those discussed previously for Intervals C and D. We therefore do not include the results in the table, since we believe

that the infrared-to-infrared lags reported in Table 3 are much more reliable indications of the behavior.

The results reported in this section strongly validate that the AGN near-IR emission is dominated by two dust components with different locations and temperatures corresponding to the sublimation of silicate and carbon grains. If the torus is perfectly face-on to the observer, the two time lags as best measured in Interval C correspond to physical scales (radii) of about 0.033 pc and 0.076 pc.

### 3.2.5. Effect of sampling cadence on lag results

To understand the errors in IR reverberation mapping, we investigated the dependence of the derived lags on the level of light curve sampling by fitting only the SAI K-band photometry (omitting that from Koshida et al. (2014)) for In-

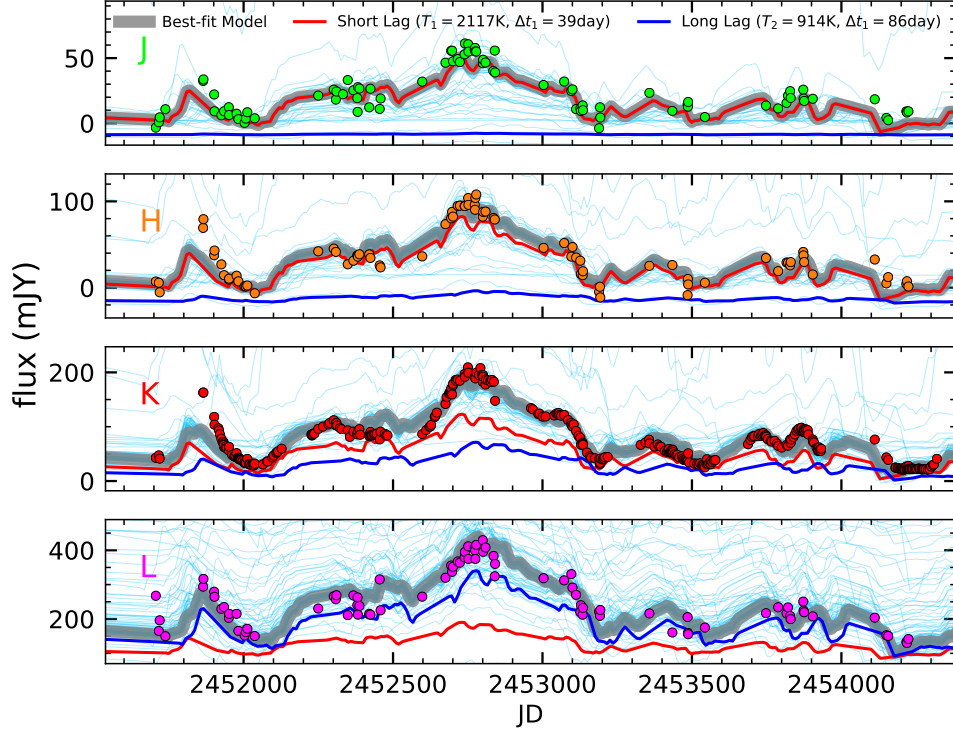


**Figure 10.** Best-fit results of all the IR light curves in Interval C with an integrated two-black-body dust reverberation model (see text for the model details). The observed light curves are shown as dots with different colors. We plot the best-fit model as a thick grey line and the contribution from the two different dust components as red and blue lines. The relative contribution of the long lag (blue line) gradually increases towards the longer wavelength and finally dominates the L-band variability.

**Table 4.** Best-fit parameter values of the model fitting all light curves in Interval C

Parameter	Prior <sup>1</sup>	Median <sup>2</sup>	MAP
$\Delta t_1/\text{day}$	$[-50, 150]$	$39.32^{+0.26}_{-0.21}$	39.37
$\Delta t_2/\text{day}$	$[-50, 150]$	$86.25^{+1.74}_{-1.92}$	85.98
$\log(AMP_1)$	$[-2, 2]$	$0.49^{+0.01}_{-0.01}$	0.49
$\log(AMP_2)$	$[-2, 2]$	$0.09^{+0.02}_{-0.02}$	0.09
$T_1/\text{K}$	$[1000, 2500]$	$2117.00^{+26.60}_{-24.72}$	2118.45
$T_2/\text{K}$	$[500, 1500]$	$913.86^{+22.42}_{-19.90}$	914.43
$F_{\text{const}}(J)/\text{mJy}$	$[-20.1, 20.1]$	$-9.05^{+0.13}_{-0.12}$	-9.02
$F_{\text{const}}(H)/\text{mJy}$	$[-29.4, 29.4]$	$-18.55^{+0.20}_{-0.22}$	-10.54
$F_{\text{const}}(K)/\text{mJy}$	$[-24.9, 74.6]$	$-1.74^{+0.63}_{-0.68}$	-1.62
$F_{\text{const}}(L)/\text{mJy}$	$[-234.3, 702.9]$	$80.26^{+7.56}_{-7.21}$	80.51

<sup>1</sup> All these priors have been sampled linearly.

<sup>2</sup> The “uncertainties” of these median values are  $2\sigma$  (i.e., 2.5%, 50% and 97.5% quantiles).

interval C. The sampling in K-band is then for the best long sequences only roughly at the Nyquist rate for the expected  $\sim 35$  day lags, with some intervals falling below this rate (and annual gaps). Although the derived temperatures for the two dust components were similar to those using the full set of data, the lags were 30 and 48 days, compared with 41 and

90 days using all the data. This result suggests that previous studies, which were generally based on relatively lower sampling cadences, may have systematic errors as a result. Such errors may account for some of the apparent changes in behavior between different time intervals (e.g., Oknyansky et al. 2014). The same concern applies to our analysis of Intervals B and D.

Where Nyquist sampling is not available, the simpler approach in Lyu et al. (2019) is preferable, namely smoothing and delaying the driving light curve to the expected behavior of the driven one, and comparing the results directly. This method strongly constrains the free parameters of the fits; e.g., it is unlikely to extract multiple lags correctly. However, the consistency of the lags derived in that work with the expected square root of luminosity scaling indicates its validity with the undersampled data available in that study.

### 3.3. Temporal Evolution of the Torus Inner Properties

Taking advantage of the  $\sim 30$ -year time coverage of the IR and optical light curves of NGC 4151, we now explore the long-term behavior of the infrared emission as an indication of possible evolution of the torus properties. As pointed out in Section 2.2, even at minimum light the  $H - K$  and  $K - L$  colors are significantly redder than expected for a normal galaxy. This behavior reveals a persistent near infrared source component that does not partake in the reverberation-mapped variability. Determining its nature is made more complex by the long-term trends in the variable flux.



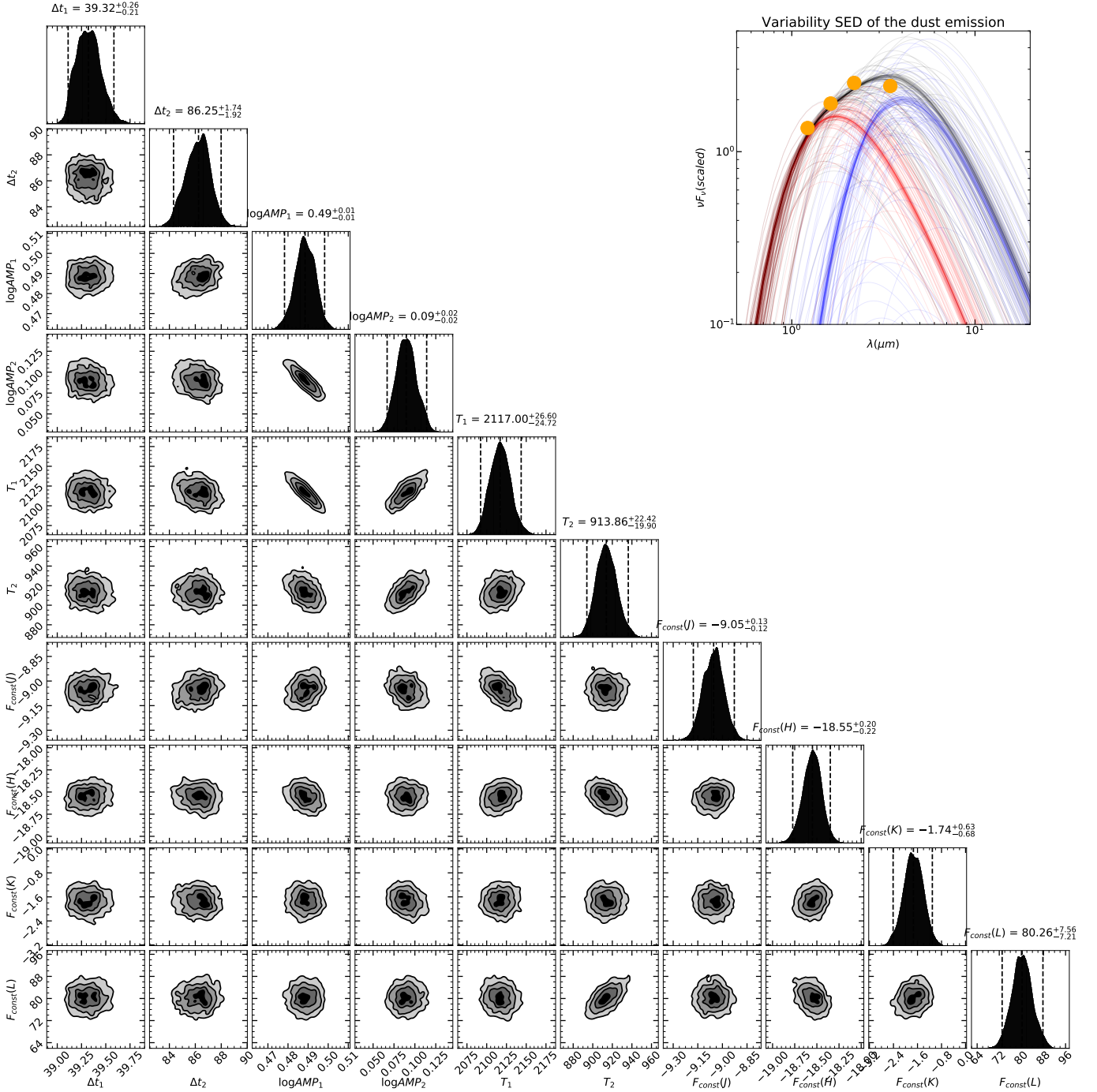


**Figure 11.** Marginalized posterior probability distributions of the fitting parameters of the integrated two-black-body dust reverberation model for light curves in Interval C. On the top of each histogram, we denote the median value of the fitted parameters with  $2\sigma$  “uncertainties” (i.e., 2.5%, 50% and 97.5% quantiles) that cover 95% credible intervals. In the top-right corner, we present the SEDs of the two best-fit black bodies (red and blue lines) and their combination (grey lines). The standard deviations of J, H, K, L light curve flux are shown as orange dots and they generally match the model prediction despite the fact that the model does not try to fit this SED directly.

**Table 5.** MAP values of the best-fit parameters from the 2-lag model fitting of individual IR light curves in different epochs

Band	$\Delta t_1$ (day)	$\log(\text{AMP}_1)$	$\Delta t_2$ (day)	$\log(\text{AMP}_2)$	$F_{\text{const}}$
Interval A: 1976/03–1980/02 <sup>1</sup>					
K	30–40	..	..	..	..
Interval B: 1994/05–2000/09					
H	32.41	-0.024	..	..	-21.75
K	27.76	0.29	..	..	5.89
L	19.52	0.49	..	..	146.95
Interval C: 2000/06–2007/05					
J	39.14	-0.30	93.78	-0.10	-8.67
H	41.97	0.16	89.45	-0.69	-9.42
K	36.43	0.43	92.28	0.29	3.43
L	31.17	0.48	92.84	0.64	107.15
Interval D: 2008/08–2016/01					
H	14.14 <sup>2</sup>	3.11e-2	..	..	-4.00e-1
K	40.36	6.50e-1	..	..	2.80e+1
L	36.22	0.63	..	..	180.58
Interval D': 2010/11–2018/08 (X-ray) <sup>3</sup>					
H	34.72	0.48	..	..	-53.05
K	36.13	0.82	..	..	-72.77
L	32.71	1.02	..	..	56.79

<sup>1</sup> As the Interval A data is composed by different datasets with very limited time sampling, the 2-lag model is poorly constrained. We only provide the possible range of the short time lags that dominate the K-band signal.

<sup>2</sup> These small lags at the shortest fitted wavelength may indicate contamination by the direct central engine signal.

<sup>3</sup> For Interval D', we have approximated the accretion disk B-band light curve by shifting and scaling the X-ray light curve to match the observed B-band light curve data and fitted the IR light curves with this synthetic B-band light curve.

We discuss this latter behavior first. Although we have successfully matched the variable component of the IR light curves with the two-lag reverberation mapping model on a 6–8 year scale, there is also a systematic trend over the full 25 year span: the variable component in B-band fades substantially more than the variable component in K-band. The top panel of Figure 12 compares the optical B and IR (J, H, K, L) light curves by normalizing to the average flux during Interval C. The B-band flux is systematically higher than the scaled IR flux in the earlier epochs but lower in the latter epochs. To extract the systematic trend between the optical and IR light curves, we fit a single lag model to the whole K-band light curve and present the best-fit results in the middle panel of the same figure. The residuals between the best-fit dust reverberation model and IR light curves show a systematic trend as a over the whole period, i.e., the model over-predicts the IR flux before Interval C but under-predicts it after. The bottom panel shows the ratio of the K-band observed flux to the best-fit K-band reverberation model, showing the increasing trend with time. An exponential fit indicates that the ratio of variable K-band to B-band flux grows by  $\sim 4\%$  per year between 1995 and 2015.

Changes in the overall levels in the K-band relative to the optical been reported previously by Oknyansky et al. (1999). They find that the K-band was reduced relative to the optical in 1995–1998 compared with 1988–1994; the end of this trend can be seen to the extreme left in Figure 12. They suggest that the change is evidence for enhanced grain sublimation during the peak in nuclear luminosity in  $\sim 1995$ . Our finding of changes over an extended time not associated with extraordinary activity in the optical suggests that there must be some other cause.

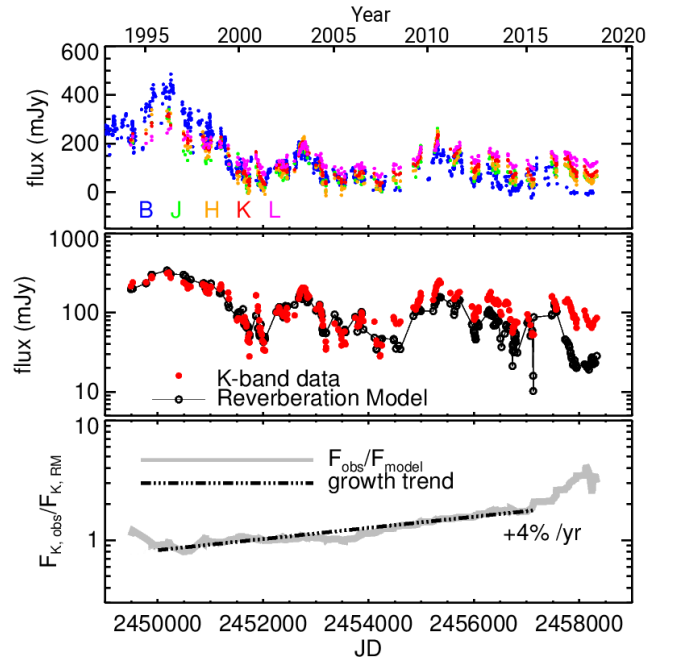


**Figure 12.** Top Panel: Comparison of the B, J, H, K, L light curves of NGC 4151. We normalized these light curves over Interval C. Middle Panel—the best-fit dust reverberation model (black open circles connected with black lines) to the observed K-band light curve over the whole observed interval (red filled dots). Bottom Panel: the ratio of the observed K-band flux to the prediction from the best-fit dust reverberation model (grey line), which assumes a constant ratio of K-band to B-band fluxes. After a period (to the extreme left) where the ratio decreases (discussed in Oknyansky et al. (1999)), the ratio increases steadily. We fit this trend with an exponential (black dot-dash line) and find a growth by  $\sim 4\%$  per year.

### 3.3.1. The Persistent Near Infrared Component

Having characterized the long-term trend in the variable emission component, we turn to the persistent one. We have assumed two subcomponents: (1) a variable one that has the same relative amplitude of variations in each band as the blue light; and (2) one that is constant in each of H, K, and L bands. We have fitted this simple model separately for each of Intervals B, C, and D, using the SAI photometry (since our method of reconciling the other sets could damp out a constant component). We required that the SED of the per-

sistent source be similar as derived individually for each of the intervals.

The result of this modeling is that the persistent source fluxes at H, K and L can be fitted by a blackbody of  $\sim 700\text{K}$ . This modeling also confirms the  $\sim 4\%$  per year growth in the variable component after 1995.

### 3.3.2. Long-term Growth of Torus Hot Dust Component

The gradually increasing near-IR flux partaking in the dust reverberation signals, as just derived, indicates either: (1) the B-band flux is not truly representative of the heating of the variable infrared component; or (2) more and more dust grains have been heated by the AGN.

We first explore whether the trend arises because the B-band has faded significantly more than the shorter wavelength (hard UV, soft X-ray) continuum that contributes to the dust heating. Interstellar dust has a broad absorption peak between  $\sim 1\text{ nm}$  and  $700\text{ nm}$  (Corrales et al. 2016). It is believed that the heating of the circumnuclear torus is from a single source component dominating the emission from the optical to the soft X-ray (Schurch et al. 2004). The nuclear continuum over this range falls roughly as  $\nu^{-1}$ , or  $\nu f_\nu \sim \text{constant}$  (Alexander et al. 1999). Assuming all of the nuclear flux is absorbed over the relevant spectral range, the heating of the circumnuclear torus is therefore roughly constant per logarithmic frequency interval.

Much of this frequency range is inaccessible due to interstellar absorption, but we can probe both the UV and soft X-ray, as shown in Figure 13. All the measurements are normalized to be of similar strength during the strong peak in emission between JD 2449000 and 2451000. With a single exception (near JD 245750, presumably an outburst), all the UV measurements appear to fade in synchronism with the B-band ones. This result is demonstrated in greater detail for NGC 5548 by Gaskell (2008), providing a useful analogy to NGC 4151. The soft X-ray measurements to some extent have their own individual excursions but still appear also to fade as in B-band. Although we cannot constrain the behavior between  $0.135\ \mu\text{m} = 135\text{ nm}$  and  $1.3\text{ keV}$  ( $1\text{ nm}$ ), the available evidence suggests that the B-band behavior is characteristic of that of the heating source of the torus hot dust emission in general, since both the UV and soft X-ray behave similarly to B-band.

We therefore attribute the increase in the variable K-band to B-band relative flux to growth in the amount of exposed dust associated with the circumnuclear torus. From the K-band emission, we estimated the hot dust mass of about  $7 \times 10^{-4} M_\odot$ . With a  $\sim 4\%/yr$  flux growth rate, the corresponding dust mass growth would be  $\sim 2.7 \times 10^{-5} M_\odot/yr$ . One possible source for these dust grains is the ultra-fast outflows in NGC 4151 (see references in Mou et al. 2017; Williamson et al. 2020). If there is torus dust lifted up by such outflows or some dust forms in-situ (Elvis et al. 2002), such excess IR emission can be expected. In fact, the typical outflow rate in the NGC 4151 nucleus is calculated to be  $3 \times 10^{-3} - 8 \times 10^{-2} M_\odot/yr$  (Mou et al. 2017). Once the gas to dust mass ratio of these clouds is below 300-8000, the re-

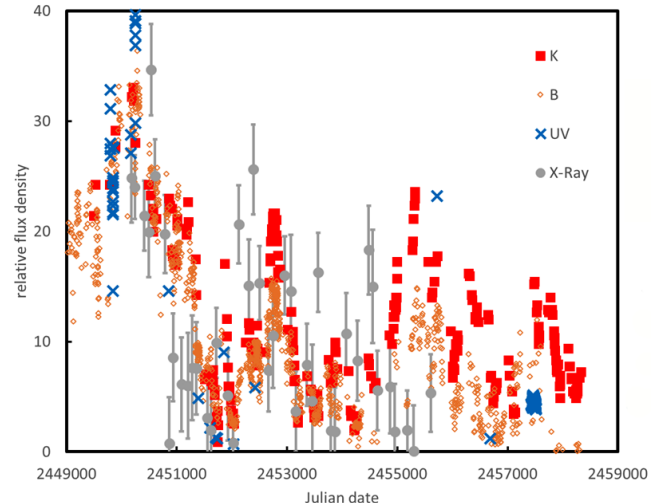


**Figure 13.** Comparison of the long-term behavior of the variable output of NGC 4151 at K, B, in the UV, and in the soft X-ray. The K-band and B-band data are as discussed previously; we have subtracted the persistent component from the K-band data and the galaxy from both. The U-band data are from Couto et al. (2016) at  $0.135\ \mu\text{m}$ , except for the final complex of measurements that are from Edelson et al. (2017) at  $0.193\ \mu\text{m}$  but are corrected to  $0.135\ \mu\text{m}$  assuming a  $\nu^{-1}$  spectrum in frequency units. The X-ray measurements are from the Rossi XTE all-sky-monitor, band A, from  $1.3\text{--}3\text{ keV}$ .

quired dust mass growth can be provided. The possibility of changes in the inner structure of the circumnuclear torus on decadal timescales due to winds and turbulence thus deserves further consideration.

Finally, the disappearance of the nucleus in the B-band at the end of the sequence we have collected (JD 2457890 and beyond in Figure 4) is highly suggestive of the hypothesis that rapid changes in the appearance of an AGN nucleus can occur due to a small BLR cloud intervening along our line of sight (Wang et al. 2012; Gaskell & Harrington 2018). The near infrared flux does not seem to react to this event. The situation can give interesting insights to the AGN behavior and furthermore emphasizes the hazards in using B-band as a reference for infrared reverberation mapping at some epochs.

### 3.3.3. Lack of Evidence for a Receding Torus

Since the optical emission of NGC 4151 has varied by a factor of seven between 1970 and 2018, the torus inner size is expected to vary by a factor of 2.6 if the dust sublimation radius follows the expected relation,  $r_{\text{sub}} \propto \sqrt{L_{\text{AGN}}}$ . However, we find an inner lag of  $\sim 30\text{--}40$  days for all four broad time intervals, corresponding to very limited variations.

To further explore if the torus size evolves with time, we divide the K-band light curve into 17 epochs with a time window of 1000 days and a step size of 500 days. Due to the relatively low-cadence sampling in these epochs, we fit a single dust lag independently to the IR data within each epoch. The

results are summarized in Figure 14 and Table 6<sup>10</sup>. The best-fit K-band time lag has a range of 30-60 days and does not follow the evolution of the optical light curve, irrespective of the smoothing window size we use ( $1/4\times$ ,  $1/2\times$  or  $1\times$ lag). These results indicate very weak, if any, evidence for a receding torus, contrary to previous conclusions in Koshida et al. (2009) and Kishimoto et al. (2013) but consistent with the results reported in Schnülle et al. (2015).

In addition, the IR-to-optical variability amplitude AMP (bottom panel of Figure 14) does not show notable correlations with the time lag, indicating the amount of dust does not change drastically on relatively short time scales following the AGN optical variability. However, the AMP value increases gradually over a 10-year scale consistent with the conclusion in Section 3.3.2.

As another test, we focus on three time windows, E1, E2 and E3, that cover the optical flux peaks at 1997, 2003 and 2011, to test if the torus structures are the same when the AGN activity is in a high state. The torus sizes for these three windows do not change within the uncertainties. The values of AMP show a steadily increasing trend, consistent with the growing torus picture.

### 3.4. Comparison with Previous Reverberation-Mapping

NGC 4151 has been the subject of extensive near-IR dust reverberation mapping programs. The SAI group has studied it in this way from the 1970s through the 2010s with J, H, K, and L band data and has reported a large range of time lag measurements from 18 days to 104 days (e.g., Oknyansky et al. 1999, 2014, 2019). A high-cadence V-K monitoring effort over 2001-2006 was carried out as part of the MAGNUM program (Minezaki et al. 2004; Koshida et al. 2009). Koshida et al. (2009) reported a time-lag variation and suggested the possibility of dust destruction and fast-reformation. Later, study by Schnülle et al. (2013, 2015) presented the results of z, Y, J, H, K band monitoring between 2010 and 2014 and reported a decreased dust lag during the observed epoch.

However, our re-analysis of the entire data set does not support a strong evolution of the torus inner size. The diverse results reported in the literature are likely a result of different methodologies of cross-correlation analysis, and/or inadequate time-sampling of the light curves.

The evidence for a wavelength dependence of the torus size is mixed. Oknyansky et al. (1999) found that the L-band lag was significantly larger than that at K-band before 1996. After 2008, the lags in the K and L-bands became similar (Oknyansky et al. 2014, 2019). Schnülle et al. (2015) found similar lags in the J, H, and K bands but rejected evidence in their data for a possible secondary longer delay in these bands during 2010-2014. Their observations did not include L-band where the longer delay becomes prominent, as shown in Figure 10. The contribution of the longer lag may not be

obvious in JHK, especially when the time-samplings of the light curves are not good enough or the intrinsic variation does not produce enough light curve features. Their result therefore does not contradict our finding of two time lags of  $\sim 40$  and  $\sim 90$  days.

## 3.5. Reverberation at 10 $\mu\text{m}$ and Longer Wavelengths

### 3.5.1. N-Band (10 $\mu\text{m}$ ): Yearly Timescales

Sembay et al. (1987) reported six “additional observations” in IRAS Band 1 (12  $\mu\text{m}$ ) over a 25 day period in 1983 and found no variations. Insight to any variability on a year-to-year timescale at N-band (10.6  $\mu\text{m}$ ) is provided by the five measurements in each of 1975 and 1976 from Rieke & Lebofsky (1981). There are no significant changes within each five-measurement sequence (see Table 2). The weighted averages for the two years are  $2032 \pm 49$  and  $2002 \pm 38$  mJy, respectively. This behavior can be compared with that of the nucleus in the B band, from Lyuty and Doroshenko (1999), with the galaxy contribution subtracted as described in that paper; the nuclear output decreased from an average of  $\sim 26$  mJy to  $\sim 12$  mJy. To compare with the behavior in the K band, for 1975 we take data from Allen (1976); Stein & Weedman (1976).<sup>11</sup> After correction for the galaxy contribution, making use of the multi-aperture photometry in McAlary et al. (1983) as well as the discussion in this paper, the average of the measurements is 195 mJy, with good agreement (peak-to-peak differences of  $\pm 15\%$ ). For 1976, we take measurements from Kemp et al. (1977); O’Dell et al. (1978) with aperture corrections and removal of the galaxy contribution as before. The average nuclear output was 124 mJy with similar scatter. The K-band measurements are not simultaneous with the N-band ones, but the 1–2 month smoothing of the K-band signal makes them representative for the times of the 10  $\mu\text{m}$  observations (see Figure 2).

While the brightness of the nucleus decreased by more than a factor of 2 at B and of 1.6 at K between 1975 and 1976, the ratio of fluxes at 10  $\mu\text{m}$  was  $0.985 \pm 0.030$ , i.e. there was no change to within a few percent. Alternatively, from Table 1, this change can be expressed as  $30 \pm 62$  mJy. If the 70 mJy change seen in K-band has a 1500K black body spectrum, a change of order 40 mJy would be expected at 10  $\mu\text{m}$ , consistent with the observations but illustrating that the hot dust that dominates at K- and L-band is not accompanied by large amounts of only somewhat cooler dust sharing its variations. That is, the 10  $\mu\text{m}$  emission is generated by a different source component, not a continuation of the one that dominates at 1–4  $\mu\text{m}$ . Consequently, the very hot dust will not contribute a significant silicate emission feature at 10  $\mu\text{m}$  because it contributes only a very small fraction of the total output at this wavelength.

### 3.5.2. N-Band: Decadal Timescales

<sup>10</sup> Since the K-band variability includes two time lags, the lag from this single lag model is systematically larger than the shorter lag (and smaller than the longer lag) reported in Section 3.2.4 and Table 5.

<sup>11</sup> The second reference only gives L-band photometry, which we correct to K-band by multiplying the flux density by 0.506, derived from the SAI photometry when the source was of similar brightness.



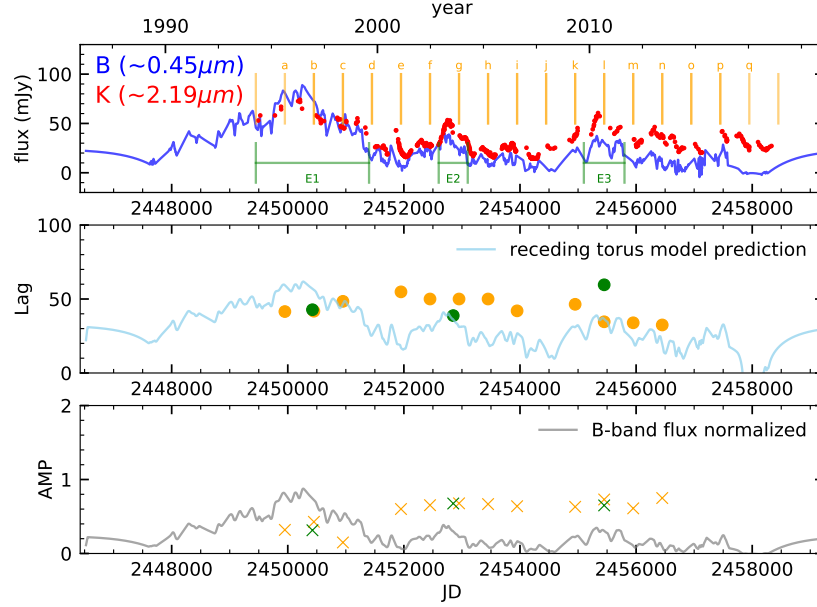


**Figure 14.** Time evolution of the best-fit single-lag dust reverberation model of NGC 4151. Top panel: the optical B-band (blue) and near-IR K-band (red) light curves and the different epochs in which the fitting is carried out. Middle panel: the evolution of the K-to-B band time lag for epoch a, b, ... q (orange dots) and E1, E2, E3 (green dots). The light blue is the expected trend if the dust lag is following a  $\Delta t \propto \sqrt{L_{\text{AGN}}}$  relation; we have normalized this relation assuming a K-band single lag of 37 days for the mean AGN B-band flux at Interval C. Bottom panel: the evolution of the relative variation amplitude (AMP). The grey line is a scaled version of the optical light curve.

**Table 6.** Best-fit Parameters of Single-lag Model Fitting at K band

epoch ID	JD range	JD (median)	1/2 lag smooth		1/4 lag smooth		1 lag smooth	
			Lag	log(AMP)	Lag	log(AMP)	Lag	log(AMP)
a	2449450–2450450	2449950	41.52	0.32	43.35	0.32	40.92	0.339
b	2449950–2450950	2450450	41.77	0.43	43.93	0.43	42.66	0.434
c	2450450–2451450	2450950	48.42	0.15	48.00	0.16	44.50	0.168
d	2450950–2451950	2451450	...	...	...	...	...	...
e	2451450–2452450	2451950	54.84	0.60	60.01	0.58	63.24	0.621
f	2451950–2452950	2452450	50.01	0.65	45.37	0.64	51.03	0.660
g	2452450–2453450	2452950	50.00	0.68	48.56	0.67	51.01	0.701
h	2452950–2453950	2453450	50.00	0.67	40.76	0.67	47.00	0.715
i	2453450–2454450	2453950	42.00	0.64	44.00	0.61	45.00	0.678
j	2453950–2454950	2454450	...	...	...	...	...	...
k	2454450–2455450	2454950	46.43	0.63	45.87	0.63	44.92	0.637
l	2454950–2455950	2455450	34.61	0.73	36.03	0.72	33.51	0.742
m	2455450–2456450	2455950	33.93	0.61	34.11	0.60	32.97	0.627
n	2455950–2456950	2456450	32.47	0.75	32.32	0.73	41.00	0.760
o	2456450–2457450	2456950	...	...	...	...	...	...
p	2456950–2457950	2457450	...	...	...	...	...	...
q	2457450–2458450	2457950	...	...	...	...	...	...
E1	2449450–2451400	2450425	42.76	0.31	45.83	0.31	41.06	0.32
E2	2452600–2453100	2452850	38.79	0.68	38.30	0.66	51.12	0.72
E3	2455100–2455800	2455450	59.60	0.65	37.23	0.70	52.99	0.69

NOTE—Due to poor time samplings and/or lack of variability features, the measurements in Epochs d, j, o, p, q have been omitted.

The relatively low luminosity and short reverberation timescales for NGC 4151 suggest that changes might be detectable at much longer wavelengths. Simple thermal equi-

librium suggests lags  $\gtrsim 3$  years at  $10 \mu\text{m}$ , so with historical observations of NGC 4151 in this band over the past 35 years, there is a chance to detect dust reverberation signals.

The top panel of Figure 15 shows a 30-day smoothed optical B-band light curve extracted from Oknyansky et al. (2016). There is a broad maximum between 1988 and 1998 with a flux increase by a factor of three. The N-band flux clearly shows a bump between 1995 and 2010 (the middle panel), as would be expected from these arguments.<sup>12</sup>

We used the B-band light curve of Figure 15 to fit the N-band light curve with a single-lag model as in Lyu et al. (2019). Given the large extent of the mid-IR emission (Burtscher et al. 2013), we used a top-hat window to smooth the B-band light curve and left the window size as a free parameter. The best-fit model, shown in Figure 15, has a reduced  $\chi^2$  of 2.78 and a smoothing window size of about 5300 days. The indicated time lag is  $2943^{+163}_{-122}$  days.

To quantify how sensitive the best-fit N-band time lag is to the smoothing effects, we arbitrarily fixed the smoothing window size to values from 100 to 3000 days and redid the one-lag reverberation fitting. The results are summarized in Table 7. The best-fit N-band lags range from 2743 to 3500 days, within the range of the reported uncertainties. If we take the extremes in the fits, a time lag between 2600 and 3600 days is indicated, corresponding to physical scales between 2.2 and 3.1 pc.

**Table 7.** Best-fit Parameters of One-lag Fitting at 10.6  $\mu\text{m}$

Smoothing Window	Lag	$\log(\text{AMP})$	$F_{\text{const}}$
(days)	(days)		
100 (fixed)	$3481^{+21}_{-21}$	$1.34^{+0.05}_{-0.06}$	$631^{+161}_{-156}$
300 (fixed)	$3488^{+72}_{-88}$	$1.29^{+0.06}_{-0.06}$	$773^{+146}_{-155}$
500 (fixed)	$3427^{+103}_{-152}$	$1.30^{+0.06}_{-0.07}$	$770^{+151}_{-155}$
1000 (fixed)	$3317^{+111}_{-121}$	$1.35^{+0.07}_{-0.07}$	$670^{+174}_{-185}$
2000 (fixed)	$2794^{+673}_{-151}$	$1.49^{+0.07}_{-0.08}$	$334^{+243}_{-252}$
3000 (fixed)	$2996^{+115}_{-154}$	$1.61^{+0.06}_{-0.07}$	$-163^{+291}_{-324}$
5341 <sup>+</sup> <sub>-360</sub>	$2943^{+163}_{-122}$	$1.87^{+0.06}_{-0.07}$	$-1899^{+561}_{-538}$

<sup>12</sup> To confirm this variability, we have carried out a  $\chi^2$  test (e.g., de Diego 2010) of the N-band data points. For a number of measurements with the flux  $f_i$  and uncertainty  $\sigma_i$ , the  $\chi^2$  is defined as

$$\chi^2 = \sum_i \frac{(f_i - \bar{f})^2}{(\sigma_i)^2}, \quad (6)$$

where  $\bar{f}$  is the average value of all the measurements. From the  $\chi^2$ -distribution, a  $p$ -value can be computed to describe the significance of the measurements randomly selected from a normal Gaussian distribution, i.e., the AGN is not variable. Since there is no evidence for variations on a yearly timescale, we combined measurements in the same year as described in Appendix B. We then obtained  $\chi^2$  (for 18 degrees of freedom, dof=18) for the N-band measurements to be 283.5 with a  $p$ -value of  $\sim 10^{-50}$ . Even if we arbitrarily increase all flux uncertainties by a factor of three, we still have a  $p$ -value of 0.007, too small for the flux variation to be due to random measurement errors. Thus, the N-band variations over decadal timescales are undoubtedly real.

### 3.5.3. Longer Wavelengths: 20–40 $\mu\text{m}$

There is no convincing evidence for reverberation-type variations at wavelengths longer than 10  $\mu\text{m}$ . At  $\sim 20$   $\mu\text{m}$ , ground-based measurement errors tend to be relatively large and there are not enough measurements distributed appropriately to make a strong statement. Although the Infrared Astronomical Satellite (IRAS) has a filter near 25  $\mu\text{m}$ , the  $\sim 0.5'$  beam is too large, making it impossible to trace AGN variability due to the contamination from the host galaxy. However, the post-2000 space-based observations from *Spitzer*, *WISE* and *AKARI* have small beam sizes of 6–12'' at  $\sim 22$ –24  $\mu\text{m}$ . We converted the measured fluxes into the equivalent values for the MIPS 24  $\mu\text{m}$  filter, making the necessary color corrections with synthesis photometry on the *Spitzer*/IRS spectrum of NGC 4151. We found  $4.27 \pm 0.05$  Jy on JD 2453013 from the *Spitzer*/IRS spectrum,  $4.13 \pm 0.05$  Jy on JD 2445498 from *Spitzer*/MIPS-24  $\mu\text{m}$  images,<sup>13</sup>  $4.00 \pm 0.08$  Jy on JD 2454876 from an *AKARI*/IRC L18W image,<sup>14</sup> and  $4.21 \pm 0.07$  on JD 2455321 from the *WISE* 22- $\mu\text{m}$  image. These values agree to within  $3\sigma$ , even without taking account of systematic errors (e.g., in the conversion to the MIPS band). Figure 15 shows this light curve does not share the falling-with-time trend in the N-band.

The measurement at 34  $\mu\text{m}$  by Rieke & Low (1975) of  $4.3 \pm 0.7$  Jy on JD 2442462 agrees well with the value of  $4.5 \pm 0.6$  Jy at 37  $\mu\text{m}$  on JD 2457436 from Fuller et al. (2019) (the radial profile in the latter reference shows that virtually the entire flux would be captured in the beam used for the former one). One additional data point can be obtained by computing synthetic *SOFIA*/*FORCAST* photometry at 37  $\mu\text{m}$  from the *Spitzer*/IRS spectrum of NGC 4151, which is  $4.7 \pm 0.2$  Jy on JD 2453013. Comparison with Figure 15 shows that these measurements span the entire duration of the 10  $\mu\text{m}$  ones and that the delayed and smoothed B-band light curve is about a factor of four lower for the most recent measurement than for the first. Again there is no sign of variability.

We conclude that IR emission at these longer wavelengths comes from a more extended dust component than that for the N-band.

## 4. PROPERTIES OF THE AGN CIRCUMNUCLEAR DUST STRUCTURES

To summarize, the torus emission in the J, H, K and L bands (1 – 4  $\mu\text{m}$ ) is contributed by three distinct dust populations. Two of these populations (at  $T \sim 900$ –1000K and  $\sim 1500$ –2000K respectively) are at nominal radii of  $\sim 0.033$  and 0.076 pc, with temperatures consistent those of sublimating graphite and silicate dust grains. A third, more persistent component has a characteristic temperature of  $\sim 700$ K. Over

<sup>13</sup> We adopted the PSF photometry from the SEIP source catalog, which is measured based on a mosaic image from two sets of observations made in May 30, 2007 and June 23, 2008. We took the median JD of these two dates.

<sup>14</sup> This measurement is based on aperture photometry, which could underestimate the source flux.

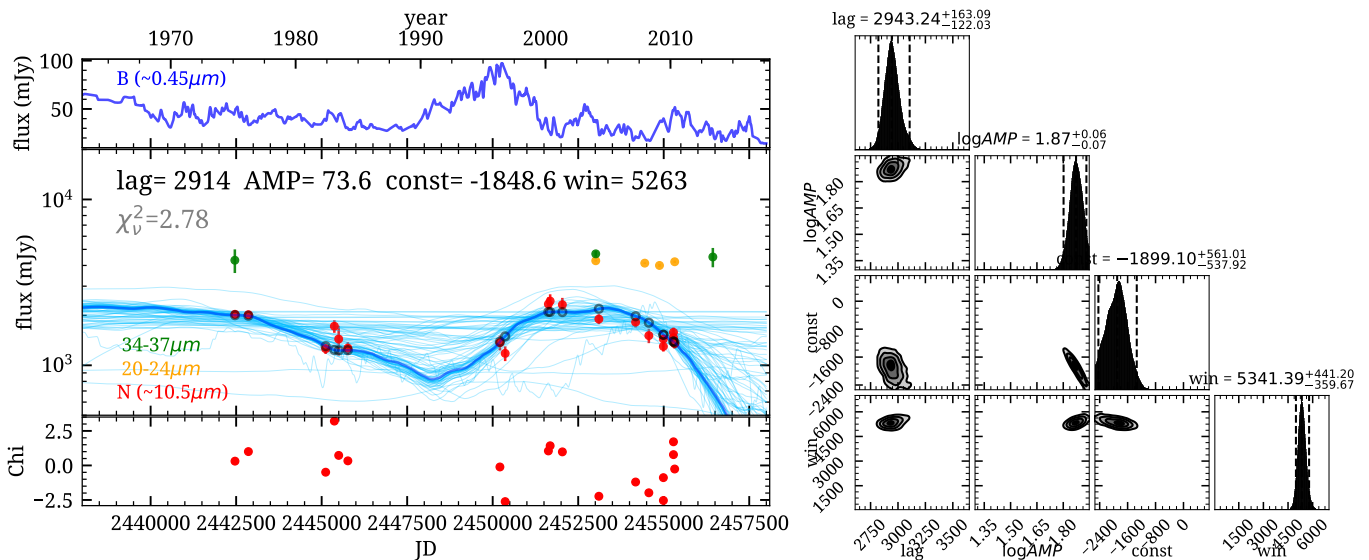


**Figure 15.** Single-lag dust reverberation model fitting of the N-band light curve of NGC 4151. On the left, the top panel shows the optical B-band light curve (blue solid line); the middle panel presents N-band (red dots), 20–24 μm (orange dots) and 34–37 μm (green dots) light curves, and the best-fit reverberation model of the N-band light curve (light blue curves); the bottom panel shows the residual of the N-band light curve fitting. Panels on the right are the marginalized posterior probability distributions of the fitting parameters to the N-band data.

a timescale of  $\sim 20$ – $25$  years, the variable component of hot dust emission has increased gradually by  $\sim 4\%$  per year compared with the B-band signal, indicating a growing inner edge to the torus. We also detect a  $\sim 10$  μm dust reverberation signal, indicating a fourth component at a nominal radius of about 2.2 - 3.1 pc. The lack of variability at 20–24 μm and 34–37 μm indicates even more extended dust structures.

In this section, we discuss these results in a broader context. We (1) compare them with other indications of the circumnuclear structure (§ 4.1); (2) use them to constrain the vertical distribution of material (§ 4.2); (3) consider them in the context of the AGN spectral energy distribution (§ 4.3); (4) use the results to confirm constraints on the dust grain sizes (§ 4.4); and (5) highlight concerns about current models (§ 4.5).

#### 4.1. Comparison of Reverberation Results with Other Observations of Circumnuclear Structures

From the reverberation behavior, the relative sizes of the three variable dust components are 75 (N-band warm dust):2.25 (sublimating silicate dust):1 (sublimating graphite dust). Given the proximity of NGC 4151, we can compare these values with size constraints on its circumnuclear dust structures from imaging and interferometry.

In the near-IR, NGC 4151 has been studied at K-band with the Keck interferometer (Kishimoto et al. 2009, 2011, 2013; Pott et al. 2010; Hönig et al. 2014). Kishimoto et al. (2013) and Hönig et al. (2014) summarize the results at 2.2 μm. The discussion in the latter paper demonstrates that the constraints on the location of the inner dust rim of the torus from reverberation mapping and those from interferometry are consistent within the uncertainties. Kishimoto et al. (2013) present a single measurement that implies the rim

has increased in size; we cannot directly test this inference, but it is of modest statistical significance and removed from any features in the B-band light curve that might be expected to accompany such an event. It does not significantly undermine our conclusion that there are no substantial changes of this nature synchronous with increases in nuclear luminosity.

At  $\sim 10$  μm, we can compare the source size derived from reverberation mapping in the N-band band with the dust size measurement with the VLTI/MIDI interferometry observations of NGC 4151 by Burtcher et al. (2009). Based on a comparison of the data to a simple Gaussian model, they inferred the emission at these wavelengths has a FWHM diameter of  $(2.3 \pm 0.5)$  pc<sup>15</sup>. To compare this measurement with the size from reverberation mapping, a number of corrections are needed: (1) from the geometry of the NLR light cones, Crenshaw et al. (2010); Fischer et al. (2013) estimate that the circumnuclear torus is inclined by  $\sim 45^\circ$  into the sky; (2) the position angle of the jet,  $77^\circ$  (Mundell et al. 2003), implies that the circumnuclear disk is only  $\sim 13^\circ$  from north-south (Kamali et al. 2019); and (3) the fitted Gaussian FWHM significantly underestimates the diameter of a disk. The first two points indicate that any disk would be fore-shortened in the direction along the interferometer baseline, which was close to east-west. With regard to the third point, the full diameter of a disk with a 70% central hole is more than 1.5 times the FWHM of a fitted Gaussian. Taken together, the FWHM from the interferometry would underestimate the diameter of a simple disk by about a factor of two. The complexities of the true nuclear structure - disk, wind, or cone - make this

<sup>15</sup> The original paper adopted a distance of 14 Mpc for NGC 4151 and reported the size to be  $(2.0 \pm 0.4)$  pc.

only a rough estimate. However, it implies that the radius of the  $10\ \mu\text{m}$  source is about equal to the quoted FWHM, which makes it similar to the radius deduced from the reverberation behavior at this wavelength.

Additional size limits on the torus size of NGC 4151 have been measured in the radio bands. With VLBA and the JVLA at 21 cm, [Mundell et al. \(2003\)](#) found the circumnuclear absorbing gas of NGC 4151 to be distributed in a thin layer of clumpy gas between the molecular and ionized gas, with the transition at  $\sim 3.9(\sin^{-1}\theta)$  pc.<sup>16</sup> This value can be treated as the upper-limit of the diameter of the compact dust torus.

#### 4.2. Circumnuclear Material Vertical Structure

Besides the source sizes and dust temperatures, our reverberation mapping also reveals information on the vertical structure. Figure 16 presents the variation amplitudes of the IR dust reverberation signals relative to the B-band variability, as a function of component distance<sup>17</sup>. More and more accretion disk emission is reprocessed into the IR bands as the dust distance increases. In addition, as shown in Section 4.1, the radius of the dominant emission component at  $10\ \mu\text{m}$  deduced from reverberation mapping is similar to that measured with interferometry. If the  $10\ \mu\text{m}$  emission region were heated via radiative transfer, its reaction would be significantly slower than speed-of-light behavior (e.g., [Guo et al. 2002](#)). Therefore, these results together indicate a vertical structure that intercepts directly the nuclear emission that powers the  $10\ \mu\text{m}$  component. This vertical height could take the form, for example, of a flared disk with clouds distributed generally above and below into the polar regions (e.g., [Siebenmorgen et al. 2015](#)) or of a dense wind feeding the NLR from the inner edge of a thin disk (e.g., [Hönig et al. 2013](#)). At our current level of understanding, the difference is largely semantic; for brevity in the following, we will describe it as a flared disk.

With some simple assumptions, we can estimate the vertical profile quantitatively. Figure 17 illustrates a simple model of a flared torus (yellow shading) surrounding a BH accretion disk (a black dot crossed over by a dark blue line). The complementary side of the sketch shows an equivalent (for our purposes) sketch of a wind model. The system has an inclination angle  $\theta_{\text{obs}}$  relative to the observer. We assume that the accretion disk emission is anisotropic and that it can be described by the model proposed in [Netzer \(1987\)](#),

$$L(\theta) = L_{\text{AD},0} \cos\theta(2\cos\theta + 1)/3 \quad (7)$$

For a specific dust component within the torus (dark green shaded region), the accretion disk can provide heating  $L_{\text{AD,DRS}}$  (“DRS” represents dust reverberation signals) only

<sup>16</sup> The original paper assumed NGC 4151 is at a distance of 13.3 Mpc and reported a size of  $3.3(\sin^{-1}\theta)$  pc.

<sup>17</sup> We have converted the optical-to-IR relative flux density variation amplitude AMP (see Equation 4) into optical-to-IR relative luminosity variation amplitude and denoted it as  $\text{AMP}(\nu F_\nu)$  or  $f_{\text{B,DRM}}$ . This parameter describes the amount of dust emission that responds to the optical variations.

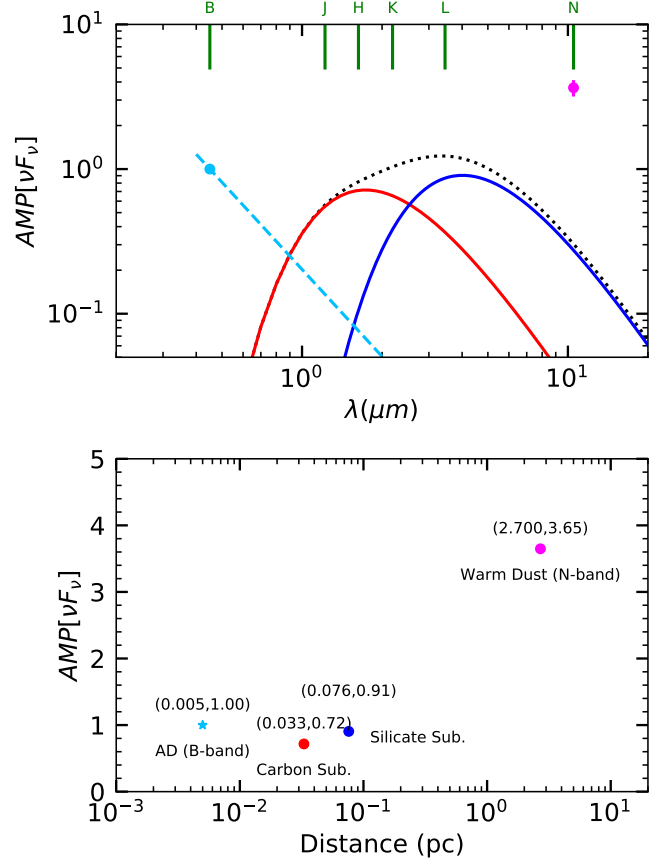


**Figure 16.** Top panel: The relative scaling factor AMP for luminosity ( $\nu F_\nu$ ) as a function of wavelength. The B-band is shown as a light blue dot with the wavelength dependence of AMP of the accretion disk as a dashed blue line. The red and blue solid lines are the two hot dust components (graphite and silicate) with their combination as a black dotted line. The N-band is shown as a purple dot. Bottom panel: The relative scaling factor AMP for luminosity ( $\nu F_\nu$ ) as a function of distance. We show the radial distance from the nucleus for each component.

through a limited range of angles  $[\theta_1, \theta_2]$  (the light blue shaded area), i.e.,

$$L_{\text{AD,DRS}} = \int_{\theta_1}^{\theta_2} dF(\theta) \quad (8)$$

Assuming  $L_{\text{AD,DRS}}$  is fully reprocessed into the IR, the corresponding total IR luminosity of this dust component is

$$L_{\text{dust,DRS}} = L_{\text{AD,DRS}} \quad (9)$$

The observer sees the B-band luminosity, whose strength is proportional to the accretion disk luminosity through the B-band bolometric correction,  $L_B = 0.2L_{\text{AD}}$  ([Richards et al. 2006](#)), thus

$$L_{\text{B,obs}} = 0.2 \times L(\theta_{\text{obs}}) \quad (10)$$



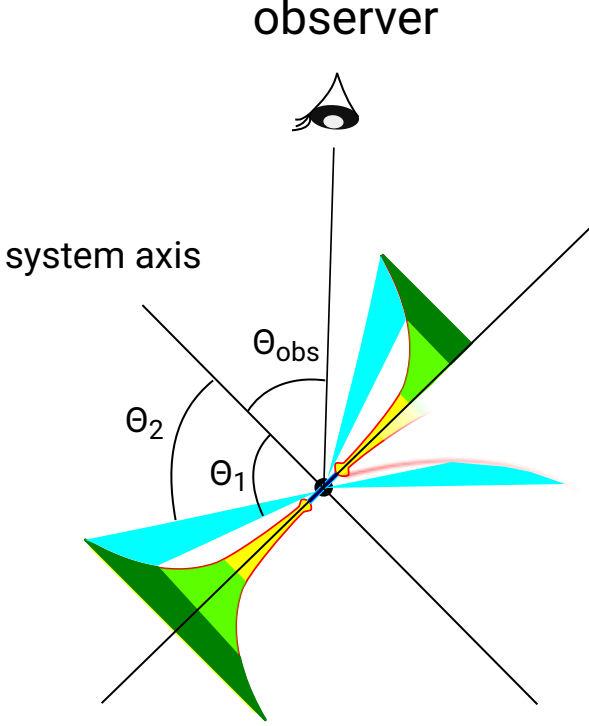


**Figure 17.** Simple geometric models to illustrate the torus vertical structures. We denote the black hole and its accretion as a big black dot crossed-over by a blue line. In the upper right case, the torus is connected to the outer part of accretion disk as a flared disk with a puffed-up inner edge (yellow shaded region). The system is inclined to the observer at angle  $\theta_{\text{obs}}$ . To aid our derivation, we highlight a dust component in the torus (dark green shaded region) with a half-opening-angle from  $\theta_1$  to  $\theta_2$ . The inner puffed-up edge shields much of the intervening torus from direct nuclear radiation. Only between these angles can the accretion disk emission (light blue shaded region) reach this dust component. See text for details. To the lower right, a wind model is illustrated. The wind is lifted from the inner, puffed-up edge and intercepts the nuclear light preferentially in the zone that dominates the emission in the mid-infrared. The puffed-up edge is the source of most of the near-infrared emission and also shields the outer zones of the narrow torus disk from direct illumination from the nucleus.

Meanwhile, the dust reverberation signals are linearly connected to the observed B-band luminosity,

$$L_{\text{IR,obs}} = f_{\text{B,DRS}} L_{\text{B,obs}} \quad (11)$$

and the  $L_{\text{IR,obs}}$  is linearly related to  $L_{\text{dust,DRS}}$  by introducing a bolometric correction to a black body spectrum associated with this dust component. From fitting observations of the narrow-line region, the inclination angle of NGC 4151 is estimated to be  $\sim 45^\circ$  (Crenshaw et al. 2010). Combining all the above equations, finally we have

$$\cos \theta (2 \cos \theta + 1) \Big|_{\theta_1}^{\theta_2} = 0.2 \times (1 + \cos 45^\circ) \times f_{\text{B,DRS}} \left( \frac{L_{\text{IR,obs}}}{L_{\text{dust,IR}}} \right)^{-1} \quad (12)$$

**Table 8.** Estimations on the Torus Vertical Structures

Component	T(K)	$f_{\text{B,DRS}}$	$L_{\text{IR,obs}}/L_{\text{dust,IR}}$	$\theta(\text{deg})$
(1)	(2)	(3)	(4)	(5)
Carbon Sub.	2000	0.72	1.00	76.4 – 90
Silicate Sub.	900	0.91	1.00	65.5 – 76.4
Warm dust	$285 \pm 12\text{K}$	3.65	1.48	23.5 – 65.5
Cold dust	$77 \pm 5$	...	...	...

NOTE—Col. (2) inferred dust temperatures from reverberation analysis and/or SED decomposition of normal AGN template; Col. (3) the fraction of energy ( $\nu F_\nu$ ) between the IR and the optical B-band variability signals as seen by the observer; Col. (4) the bolometric correction of the observed IR band to the integrated black-body spectrum with dust temperature in Col. (3); Col. (5) the range of dust half-opening angles as derived in Equation 12.

The results are summarized in Table 8. With increasing distance (and resulting decrease in dust temperature), the dust components receive the accretion disk emission from smaller inclination angles, consistent with the flared torus picture. The minimum value of  $\theta$  for the warm dust component defines the half-opening angle of the torus to be  $\sim 23^\circ$ . This value is very approximate; for example, it depends on the assumed anisotropy of the accretion disk emission. Nonetheless, it is consistent with the average value of the  $15\text{--}33^\circ$  half-opening angle of the narrow line region bi-cone in NGC 4151 as inferred by Das et al. (2005); Fischer et al. (2013). In addition, assuming the torus obscuration is the main driver for the different AGN types, this number corresponds to the  $\sim 30\%$  fraction of type-1 AGN, which is roughly consistent with observations for an AGN with  $L_{\text{bol}} = 10^{43.8}$  erg/s as in NGC 4151 (e.g. Schmitt et al. 2001).

#### 4.3. Linking Dust Reverberation Signals to the IR SED

We now test whether the picture of the torus derived above is consistent with the spectral energy distribution (SED) of the AGN, shown in Figure 18. The SED is generally measured with sufficiently large fields of view to capture the emission from polar dust as well as from the torus. The 2–5  $\mu\text{m}$  spectral bump is characteristic of a *normal* infrared SED in the terminology of Lyu et al. (2017) and indicates that the polar dust contribution at these wavelengths is small (Hönig & Kashimoto 2017; Lyu & Rieke 2018). However, it can be larger, even dominant, at the longer wavelengths.

Radomski et al. (2003) resolved 506 mJy of polar dust with spatial resolution  $\sim 0''.55$  (diameter); if we apply the photometric correction for their wide spectral band, this becomes 630 mJy. To estimate a total, we have assumed that the polar infrared emission is proportional to that in the  $[\text{O III}]\lambda 5007\text{\AA}$  line and used the slit fluxes of Das et al. (2005) to determine how much additional emission is likely inside of  $0''.3$  (radius), leading to a total flux of 0.9 Jy. The model of Burtcher et al. (2009) finds  $0.70 \pm 0.16$  Jy in a  $\sim 30$  mas ( $\sim 2.3$  pc) FWHM Gaussian and 0.2 Jy in a central point source; if we combine these values with the 0.9 Jy measured by Radomski et al. (2003) (corrected) in a more extended

component, we account for the  $\sim 1.8$  Jy total flux at the time of the [Burtscher et al. \(2009\)](#) measurements (JD 2454579; see Table 2). This polar dust component extends to  $\sim 200$  pc ([Radomski et al. 2003](#)); only the inner  $\sim$  half of the flux ( $\sim 0.9$  Jy) can contribute to the N-band variations.

The left panel of Figure 18 shows the SED of NGC 4151 and our best-fit empirical model, which reconciles the mid-IR polar emission with the range of type-1 AGN IR SEDs observed at  $z \sim 0-6$  and with the commonly seen UV-optical obscuration ([Lyu & Rieke 2018](#)). The AGN-heated dust emission can be described by two components: (1) the traditional relatively compact torus (without dust along the polar direction) whose face-on SED is described by a small set of AGN intrinsic SEDs ([Lyu et al. 2017](#)); and (2) extended infrared optically-thin polar dust with its emission SED peaked around  $25-30 \mu\text{m}$  and strength typically represented by an effective optical depth  $\tau_V$ . The validity of this model is confirmed by the close match of  $10 \mu\text{m}$  polar emission strengths from our SED model and those from mid-IR interferometry of galaxies where it is available. The SED decomposition suggests polar dust emission of optical depth  $\tau_V \sim 0.75$  as in [Lyu & Rieke \(2018\)](#). The nuclear/torus contribution is 56% of the total  $10 \mu\text{m}$  flux density, or for the measurements used in the fit, accounts for 1 Jy of the output, with  $\sim 0.8$  Jy from the polar dust. These values are consistent with those derived above from the observations.

To identify the major dust components in the torus, in the right panel of Figure 18, we decompose the IR emission of the normal AGN intrinsic SED into several black/grey body spectra after subtracting a broken power-law component that represents the accretion disk. The greybody spectra are a useful approximation because the disk temperature can drop precipitously inside the inner edge of the disk in full radiative transfer models (see, e.g., Figure 3 in [Venanzi et al. \(2020\)](#)), which is combined with the  $T^4$  dependence of the emitted luminosity. This behavior is supported in our work by the lack of response at  $10 \mu\text{m}$  to variations detected in the K-band. Thus, where a disk inner edge is set by grain sublimation, the greybodies are not only a reasonable approximation to the total emission, but also are characteristic of dust close to the sublimation temperature.

The fit fixes the hottest dust emission at a temperature of  $T \sim 2100\text{K}$ , with the best-fit values for the other dust components of  $\sim 890$ ,  $285$  and  $85$  K, confirming that the  $1-4 \mu\text{m}$  emission is dominated by two distinct dust components close to the sublimation temperatures of graphite and silicates<sup>18</sup>. For the component that dominates the emission at  $8-20 \mu\text{m}$ , we obtain a dust temperature of  $285\text{K}$ . [Burtscher et al. \(2009\)](#) reported a similar color temperature from the  $0.3''$ -aperture

<sup>18</sup> The  $T \sim 2100$  K temperature of the hottest dust component is higher than the typical value of  $\sim 1800$  K assumed for the dust sublimation of graphite (e.g., [Barvainis 1987](#); [Mor et al. 2009](#)). However, the higher temperature may be a result of stochastic heating of transient very small graphite particles as discussed in the next section. Alternatively, this temperature may result because the dust sublimation zone is likely adjacent to the gas in AGN broad-line regions ([Baskin & Laor 2018](#)).

( $\lesssim 23$  pc) MIDI mid-IR spectrum of NGC 4151. We conclude that the N-band dust reverberation signals are dominated by this component. If we use the wind temperature relation from [Venanzi et al. \(2020\)](#), put  $r_{sub}$  at  $0.076$  pc from the reverberation behavior, and assign a temperature there of  $1000$  K, we find that the temperatures dominating at  $10 \mu\text{m}$  are at  $2.0$  ( $310\text{K}$ ) to  $3.6$  ( $250\text{K}$ ) pc. This behavior agrees perfectly with expectations from the N-band lag determination. Of course, this emission is only one component of the polar emission; the much more extended flux ([Radomski et al. 2003](#)) must arise from stochastically heated grains or grains heated locally, e.g., from hot gas.

The cold dust component in the far-IR is characterized by a gray body at  $T \sim 85\text{K}$ . Given the similar far-IR SED shapes of various types of AGN, this emission is likely to be optically-thin and very extended ([Lyu & Rieke 2017](#)). It probably originates in very extended polar dust. The lack of variability at  $20-24 \mu\text{m}$  and  $34-37 \mu\text{m}$  (see Section 3.5.3) supports the conclusion that this spectral range is dominated by these very extended dust components.

In conclusion, the AGN-heated torus emission of NGC 4151 can be characterized by five dust components. The first two correspond to graphite and silicate grains in the dust sublimation zone of the AGN torus, the third provides persistent emission at an apparent temperature of  $\sim 700$  K, the fourth is at  $\sim 285$  K and between  $2.2$  and  $3.1$  pc from the nucleus, and the fifth is at  $\sim 85$  K and is extended up to  $\sim 200$  pc; it contributes the far infrared emission. These results are only rough estimates. In more realistic cases, one would need to build a detailed dust radiative transfer model to match the dust reverberation constraints as well as the SED and consider the optical thickness of the clouds, the inclination angle effect, the anisotropy of the accretion disk emission, etc. The left panel of Figure 18 shows that the SED from an existing radiative transfer model agrees closely with our empirical one, but the new information from the lag analysis can support further refinement. Such modeling efforts are beyond the scope of this paper.

#### 4.4. Properties of Dust Grains

It is likely that the dust near an AGN can only survive in large grains ([Laor & Draine 1993](#); [Maiolino et al. 2001](#); [Baskin & Laor 2018](#)). Our observations, which locate the sublimating grains in distance from the accretion disk, support this conclusion. We take the bolometric luminosity of NGC 4151 to be  $7 \times 10^{43} \text{ erg s}^{-1}$  from the  $\lambda F_\lambda(5100\text{\AA})$  flux ([Kaspi et al. 2005](#)). Adopting  $F_{UV} = 0.165 F_{tot}$  ([Risaliti & Elvis 2004](#)) and putting the dust grains at their typical sublimating temperatures ( $T_{sub,S} \sim 1000\text{K}$  and  $T_{sub,C} \sim 1500\text{K}$ ), equations 1, 2 give minimum survival grain sizes and can be written as

$$R_{sub,C} = 0.044 \left( \frac{a_C}{0.05 \mu\text{m}} \right)^{-0.5} \text{ pc} , \quad (13)$$

$$R_{sub,S} = 0.092 \left( \frac{a_S}{0.05 \mu\text{m}} \right)^{-0.5} \text{ pc} , \quad (14)$$

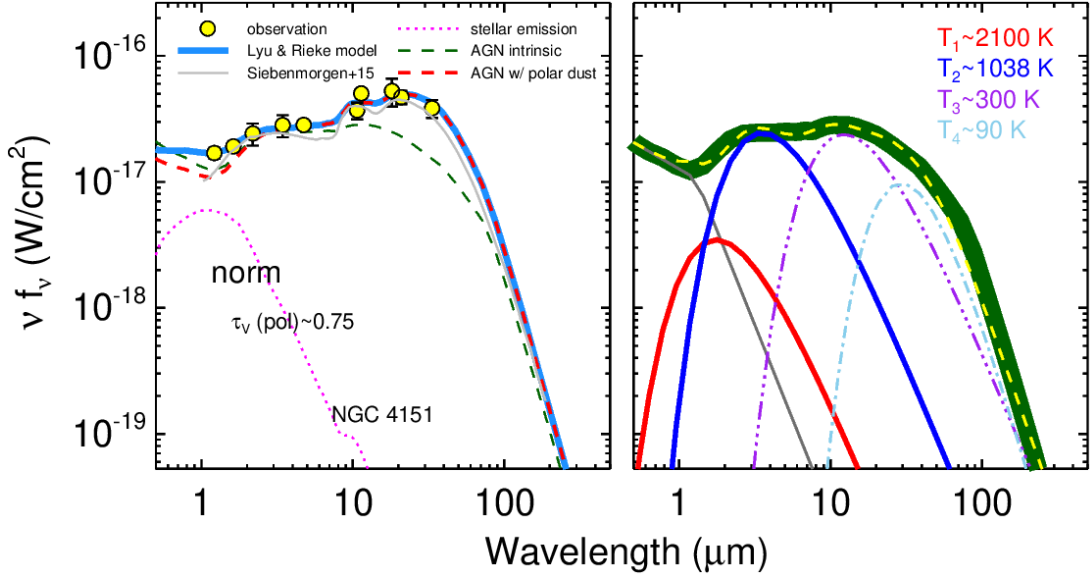


**Figure 18.** Left panel: Best-fit results of the AGN IR SED of NGC 4151 with the semi-empirical model presented in Lyu & Rieke (2018). The photometry data (yellow dots) was taken from Alonso-Herrero et al. (2003). The SED model (blue thick solid lines) is composed of the AGN component (red dashed line) and the stellar component (magenta dotted lines). We also plot the corresponding intrinsic AGN template before polar dust obscuration (green dashed line). As an comparison, the grey line is the dust radiation transfer model SED for NGC 4151 in Siebenmorgen et al. (2015), shifted down slightly so it is not obliterated by our empirical fit. Right panel: Dust component decomposition of the normal AGN intrinsic template. The final model (yellow dashed lines) includes a broken power-law component to represent the accretion disk emission (gray solid line), three black body spectra (red solid line; blue solid line; purple dashed-dotted-dotted-dotted line) and one gray body spectrum (light blue dashed-dotted line) to characterize the torus dust emission. We have fixed the temperature of the hottest dust component at 2100 K and summarize the best-fit temperatures in the top-right corner of the panel.

The two time lags as measured in Interval C correspond to physical scales of about 0.033 pc and 0.076 pc, which would suggest grain sizes of  $\gtrsim 0.07\text{--}0.08\ \mu\text{m}$  for both graphite and silicate grains. These inferred grain sizes are an order of magnitude larger than typical small grains in the classical diffuse ISM (e.g., Weingartner & Draine 2001).

Erosion of these large grains will yield a transitory population of very small refractory grains, composed both of carbon and of very small grains of refractory oxides such as FeO and MgO (Mann et al. 2007). Such grains can be heated stochastically above their thermal equilibrium values (Manske & Henning 1999; Draine & Li 2001), consistent with the high temperature for the hottest dust in the SED fitting in the previous section.

#### 4.5. Variability/Lag Behavior Compared with Torus Models

Given the constraints on the AGN dust structures in NGC4151 obtained above, we now examine the assumptions and basic features of some popular torus models. The following discussion will highlight areas where refinement is recommended in the future modeling work.

##### 4.5.1. Challenges to the Clumpy Torus Models

Many previous studies of circumnuclear tori have used *geometric/ad hoc models*, in the nomenclature of Ramos Almeida & Ricci (2017). Such models fit the infrared SED by assuming a quasi-static dust distribution (e.g., smooth,

clumpy, or a combination) and a grain composition. The most popular class of model posits the torus to be in the form of many individual gas/dust clouds with little material in between, hence the term “clumpy” models. Such tori were modeled extensively by Nenkova et al. (2008a,b), whose results (and subsequent elaborations) are widely used to analyze various AGN IR observations. As summarized in the abstract of Nenkova et al. (2008a) — “in a clumpy medium, a large range of dust temperatures coexist at the same distance from the radiation central source.” — a major feature of these models is that individual optically-thick clumps emit at a broad range of temperatures due to the effects of radiative transfer, so that the emission at different wavelengths can come from the same clumps, making a relatively compact torus (Nenkova et al. 2008a).

The behavior of NGC 4151 appears to be inconsistent with the predictions of these models in two ways:

**10–30  $\mu\text{m}$  Reverberation Behavior:** Almeyda (2017a); Almeyda et al. (2017b, 2020) investigated extensively the infrared reverberation response of the Nenkova et al. (2008a,b) clumpy models from a theoretical perspective, providing a useful comparison for our study. In particular, their work focused on NGC 6418, a type 1 AGN quite similar to NGC 4151, with about 1/3 the luminosity and a reverberation lag time at 3.6  $\mu\text{m}$  of about 37 days (Vazquez 2015), i.e. about 40% that for NGC 4151 at this wavelength (roughly consistent with the expected luminosity scaling). Given their over-

all similarity, the conclusions for NGC 6418 should also apply with suitable scaling to NGC 4151.

Given the general characteristic of clumpy models that each clump contains a broad range of temperatures and hence emits over a broad range of infrared wavelengths, the relative delays from one infrared wavelength to another are small in these models. The highest fidelity models, for anisotropic torus illumination and full radiative transfer, show simulated lags of 31.46, 33, 35.97, and 55.91 days respectively for 2.2, 3.6, 4.5, and 10  $\mu\text{m}$  (Almeida 2017a). Although the response curves are smoothed increasingly with increasing wavelength, over the 2.2–10  $\mu\text{m}$  range, they track each other well. Other than short periods of mismatch due to different response times, the fractional change in the baseline flux at 10  $\mu\text{m}$  is 80–100 % of the fractional change of the baseline at 2.2  $\mu\text{m}$  (Almeida 2017a).

The behavior we have found for NGC 4151 is in poor agreement with these predictions. For example, in Figure 19 we compare the K-band photometry (delayed by 30 days roughly as predicted by the models) with the 10  $\mu\text{m}$  measurements. They strongly disagree. In Section 4.3 we show that about half of the 10  $\mu\text{m}$  flux originates in the compact source responsible for the reverberation behavior. It is not plausible that the behavior shown in Figure 19 could hold, even if half of the 10  $\mu\text{m}$  signal is varying synchronously with the K-band signal and with 80–100% of its relative (to the baseline flux) amplitude, while the other half of the signal is constant, e.g. from very extended polar dust.

The set of 10  $\mu\text{m}$  measurements in 1975 and 1976 can be used for another test of clumpy models. Taking the flux from the nucleus (i.e., eliminating the contribution of any polar dust, see Section 4.3) to be 1000 mJy, the measurements put an upper limit ( $3\sigma$ ) of 220 mJy on any decrease from 1975 to 1976. The change between these two years in K-band is a decrease of  $\sim 36\%$ . Assuming that the fractional change at 10  $\mu\text{m}$  is  $\geq 0.8$  as large (Almeida 2017a), we would expect a change of  $\geq 290$  mJy, well above the  $3\sigma$  upper limit.

In Lyu et al. (2019), we reported the lack of variability at 24  $\mu\text{m}$  over multi-year timescales for low-redshift quasars. We found that this behavior is also likely to be inconsistent with pure clumpy torus models, although this conclusion was backed by less detail than for NGC 4151. Combining the studies, we conclude that these models have significant issues for modeling the global infrared emission of AGNs, although many aspects of them are still likely to be relevant. A likely possibility is that they leave out components that are responsible for the longer wavelength infrared emission, which might be extended and diffuse such as winds and polar dust (see next section).

Treatment of the Dust Sublimation Zone: The Nenkova et al. (2008a,b) clumpy models have a simple and sharp cut of the dust distribution without discerning the different sublimation radii of graphite and silicate grains. Such pure *clumpy* models have difficulty fitting the 1–4  $\mu\text{m}$  output of AGNs (Mor et al. 2009; Hernán-Caballero et al. 2016). Mor et al. (2009) introduced a hot black body component (associated

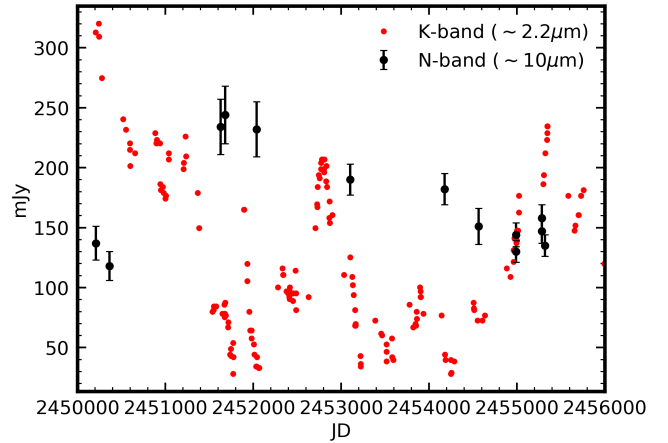


**Figure 19.** Light curve at K (red) compared with 10  $\mu\text{m}$  measurements (black; the former delayed by 30 days and the latter renormalized to bring them onto the same scale). Although models for the reverberation behavior predict that the behavior at these two wavelengths should be very similar (Almeida 2017a), the measurements show very little resemblance.

with sublimating graphite dust) to achieve adequate matching. Recently, Almeida et al. (2020) found the predicted torus sizes at 2.2  $\mu\text{m}$  from the Nenkova et al. (2008a,b) models are typically a factor of  $\sim 2$  larger than the constraints from previous K-band reverberation mapping and argued the existence of a graphite-dominated torus innermost region. Our finding of two distinct dust time lags in the near-IR emission of NGC 4151 strongly support the existence a graphite-only region, which should be considered in future improvements of clumpy models.

#### 4.5.2. Other Torus Models

The polar opposite to clumpy models is smooth ones, exemplified by those of Fritz et al. (2006). A number of issues with these models led to the development of the clumpy ones (Nenkova et al. 2008a,b). In addition to contradicting observations of clumpy structure in some galaxies, very generally these models have difficulty fitting the mild silicate (emission or absorption) features in AGN SEDs. The behavior of NGC 4151 at 10  $\mu\text{m}$  raises another concern. In the Fritz et al. (2006) models, the SED is generated by a range of temperatures throughout the torus, with outer radial zones heated by radiative transfer, which should be significantly slower than direct radiation. This picture is difficult to reconcile with the variability at 10  $\mu\text{m}$ , and particularly with the apparent agreement in the size of the 10  $\mu\text{m}$  source from the reverberation behavior with that measured through interferometry, as discussed further in Section 4.1.

The mixed clumpy/smooth torus models of Stalevski et al. (2012) appear to retain the advantages of the clumpy torus models but with the additional smooth component needed to fit the hot dust emission. The overall success of these models relative to our results depends on the structure that dominates the reverberation behavior at 10  $\mu\text{m}$ . In the models, much of



the  $10\ \mu\text{m}$  flux is generated in the clumps (see their Figure 5) and will have reverberation behavior similar to that at shorter wavelengths. We find that the variable  $10\ \mu\text{m}$  flux arises from a much more extended component, posing a challenge for the Stalevski et al. (2012) models as well.

In addition, the predicted torus inner size of such two-phase models based on SED analysis of NGC 4151 is systematically larger than the observational constraints from near-IR dust-reverberation mapping and interferometry observations. Swain et al. (2021) have introduced an additional graphite ring-like structure between the torus and the accretion disk, and carried out a full 3D radiative transfer model of the NGC 4151 IR SED. They conclude that the graphite ring has an inner radius of  $\sim 0.04\ \text{pc}$  ( $= 48$  light days) and that there is an outer disk of normal ISM dust with an inner edge at  $\sim 0.1\ \text{pc}$  ( $= 120$  light days), i.e. within uncertainties in excellent agreement with our reverberation analysis values of  $0.033$  and  $0.076\ \text{pc}$ , respectively. Nevertheless, the detailed geometry of torus inner structures can be more complicated. For example, it is proposed that the inner ring might be puffed up due to radiation pressure (e.g., Krolik 2007; Hönic 2019).

Besides the classical perception of a compact torus, the winds feeding the polar dust (Hönic et al. 2013) are also candidates to account for the  $10\ \mu\text{m}$  reverberation behavior. The physics of these winds is described by Venanzi et al. (2020). A suite of radiative models has been presented by Hönic & Kashimoto (2017) that predict the mid-infrared spectra of these winds and specifically fit the SED of the wind-dominated case of NGC 3783. Although the emphasis in these models is polar dust at relatively large distances from the nuclear engines, they should contain dust at the appropriate distance and directly illuminated by the accretion disk, as needed to account for the  $10\ \mu\text{m}$  variations.

These models are parameterized in terms of  $\alpha_{IR}$ , the spectral index between  $3$  and  $6\ \mu\text{m}$ , and  $\alpha_{MIR}$ , the index between  $8$  and  $14\ \mu\text{m}$ . The latter is  $\sim -1.5$  from the IRS spectrum (Weedman et al. 2005). The former is more difficult to constrain; simultaneous observations (to avoid effects from variability) are generally not available at either wavelength, and the one exception, the ISO SWS spectrum, is of poor quality at  $6\ \mu\text{m}$ . A value of about  $-1$  to  $-1.2$  is indicated. These values place NGC 4151 in the region where strong silicate emission is expected (Hönic & Kashimoto 2017), whereas none is seen in NGC 4151 (Weedman et al. 2005). Further analysis should clarify the role in the  $10\ \mu\text{m}$  variability of optically thin dust clouds in the wind.

#### 4.6. Other Aspects of Torus Behavior

##### 4.6.1. Variations not Described by Geometric/Ad Hoc Models

The three *geometric/ad hoc* model types just discussed all describe a quasi-static torus, i.e., they do not include mechanisms to account for changes on decadal timescales. However, as presented in Section 3.3.2, the hot dust emission strength has gradually increased over two decades, whereas in the previous  $\sim 4$  years it had been decreasing (Oknyansky et al. 1999).

Possible physical insights into this behavior can be gained from *physical* models. In fact, the AGN torus is a violent environment featuring both inflow and outflow, a dynamic aspect that emerges in various hydrodynamical simulations (e.g., see references in Netzer 2015). After considering both stellar and AGN feedback, the simulations of Wada (2012) establish the circumnuclear torus as being dominated by turbulence and transitory density enhancements (i.e., “clumps”) embedded in a smoother gas distribution. The density contrast between the components is a factor of a few. They predict turbulence and winds continuously lifting significant amounts of material off the torus, which would naturally explain long term trends such as the growing (and variable) hot dust emission, as well as the maintenance of the polar dust.

Evidence for a turbulent torus with outflow/inflow signatures has been seen in a few nearby AGNs at submm and mm wavelengths. With the high-spatial resolutions achieved by long-baseline interferometry, water maser emission in Circinus galaxy and NGC 3079 shows a compact structure with possible signatures of outflows (Greenhill et al. 2003; Kondratko et al. 2005). ALMA observations have revealed a turbulent circumnuclear structure with complicated dynamical motions in NGC 1068 (e.g., García-Burillo et al. 2016, 2019; Gallimore et al. 2016; Imanishi et al. 2018) and some other AGNs as well (e.g., Alonso-Herrero et al. 2018).

##### 4.6.2. The lack of adjustment to changes in nuclear luminosity

It is well-established that the time lag for hot dust at the inner edge of the torus is strongly correlated with AGN bolometric luminosity, following  $\Delta t \propto \sqrt{L_{\text{AGN}}}$  (e.g., Oknyansky & Horne 2001; Koshida et al. 2014; Lyu et al. 2019; Minezaki et al. 2019). However, we found in Section 3.3.3 that no significant changes of this type are seen. Evidently the relaxation to the usual relation with luminosity proceeds slowly (at least more slowly than over a decade).

In fact, due to its high optical depth the underlying disk in the dusty torus will be relatively robust against erosion. Since the torus inner edge is optically thick, changes will propagate at the sound speed of turbulent gas within the torus, which is expected to be  $20\text{--}100\ \text{km s}^{-1}$  (e.g., Hopkins et al. 2012). A size change of  $10$  light days would typically require  $16\text{--}80$  years to re-establish the equilibrium structure. In addition, much of the hot dust emission may come from dusty clouds lifted by turbulence above the torus. Their destruction is only on a timescale of a decade or longer under the direct exposure to AGN radiation (Namekata et al. 2014). In addition, to first order the process of turbulence lifting dust out of the torus will continue roughly continuously (e.g., described as a “fountain-like” structure in Wada (2012)), further reducing the chance to detect notable structure changes.

Only on these longer timescales should we expect the underlying dusty disk to retreat under increased nuclear luminosity and its infrared emission to reach the relation  $\Delta t \propto \sqrt{L_{\text{AGN}}}$ .

##### 4.6.3. The Similarity of AGN Torus $1\text{--}5\ \mu\text{m}$ SEDs Results from Dust Properties

The torus emission at 1–2.5  $\mu\text{m}$  is dominated by carbon dust near its sublimation temperature, while the emission at 2.5–5  $\mu\text{m}$  adds a substantial contribution from silicate dust. Because the torus is optically thick, the emission will be dominated by dust just behind the sublimation radii and close to the sublimation temperatures. The relative abundances of these materials should also be similar for the circumnuclear environments of most, if not all, AGNs. As a result of the similar temperatures, positions, and compositions of the emitting dust, there should be a generally similar SED for AGNs from 1–5  $\mu\text{m}$ . This result is confirmed by observation (Lyu & Rieke 2017); the variety in SEDs can be traced to (1) the amount of emitting material in the inner torus, with hot-dust-deficient (HDD) SEDs resulting from low-dust-mass cases; and (2) the relative amounts of material at large radii, with warm-dust-deficient (WDD) SEDs resulting when the outer parts of the torus and/or the winds feeding the polar dust are reduced.

## 5. CONCLUSION AND SUMMARY

We have conducted a comprehensive study of the dust reverberation signals at  $\lambda \sim 1\text{--}40 \mu\text{m}$  from the famous type-1 AGN in NGC 4151, covering a time-frame of 30–40 years. Although a number of reverberation studies in the near-IR have been published previously, they are each based on a limited subset of the available data and only probe the very inner part of torus. By analyzing all the light curve data at 1–4  $\mu\text{m}$  and literature measurements at 10–40  $\mu\text{m}$ , we have been able to identify two lags corresponding to the sublimation radii of carbon and silicate dust, respectively, plus a third lag for cooler dust at  $\sim 285 \text{ K}$ . This approach has led to a deeper understanding of the circumnuclear dust structures.

We have identified several issues that have might affect previous optical-IR correlation analyses, i.e.,

- The deduced reverberation delays are sensitive to the observation cadence, and can be affected even in some of the individual highest-cadence studies: §3.2.5.
- Although the optical and blue photometric bands are frequently used as proxies for the UV spectral component that heats the circumnuclear dust, these bands sometimes show behavior that is not reflected in the behavior of the torus: §3.1.2.

To eliminate effects of the first type, we have focused our analysis on a seven-year period (June 2000 - August 2007) when multiple campaigns can be combined to provide well sampled light curves in both B-band and in the near infrared. To mitigate issues of the second type, we first measured relative dust time lags of the J, H, K and L bands (1.25 – 3.6  $\mu\text{m}$ ) relative to each other as the dust emission variability at these wavelengths shares the same physical mechanism. We then measure the lag of K relative to B, since these two bands have the highest measurement cadences. In addition, we have also developed physical guidelines to fit all the IR light curves simultaneously to reveal the physical properties of the underlying dust components.

As the results from this work cover a large range of scales and behavior, we will organize the summary of our scientific conclusions around Figure 20.

### 5.1. Panel (a), the Surrounding Galaxy

- There are apparent outbursts in the B-band that do not create a reaction of reradiated infrared emission; they might arise from supernovae or other activity in the surrounding galaxy: §3.1.2.
- Even with imaging data, there are significant discrepancies in estimates of the galaxy infrared flux that needs to be subtracted to get a pure nuclear flux. We demonstrated a J – H vs. H color-magnitude technique that allows accurate estimation of the galaxy flux: §2.2.

### 5.2. Panel (b), the NLR and Polar Dust

- The lack of variations on decadal timescales at 20 – 40  $\mu\text{m}$  (§3.5.3) indicates this emission originates far out in the polar dust, which is observed to extend to a  $\sim 100 \text{ pc}$  scale and also accounts for up to about half the 10  $\mu\text{m}$  emission (Radomski et al. 2003; Lyu & Rieke 2018): §4.2.

### 5.3. Panel (c), the Circumnuclear Torus

- The variability of about half of the 10  $\mu\text{m}$  flux (§3.5.2) is consistent with it arising between about 2.2 and 3.1 kpc from the nucleus, possibly in the direct wind leaving the inner edge of the torus, although there could be a contribution from a large flared torus: §4.2.
- From the variability amplitudes, we estimated the half-opening angles of the different dust components, with sublimating graphite dust at  $\theta \sim 76\text{--}90^\circ$ , sublimating silicate dust at  $\theta \sim 66\text{--}76^\circ$ , and  $\sim 10 \mu\text{m}$  warm dust component at  $\theta \sim 24\text{--}66^\circ$ , i.e., a torus half-opening angle of  $\sim 23^\circ$ . This estimate agrees well with the half-opening angle of the narrow-line region bi-cone in NGC 4151, which is  $15\text{--}33^\circ$ , with an average value equal to the minimum half-opening angle of this warm dust component Das et al. (2005); Fischer et al. (2013): §4.2.
- The range of time lag behavior between 1.2 and 10  $\mu\text{m}$  and the lack of IR variability at 20–40  $\mu\text{m}$  show that the hot, warm and cold dust emission originates over a large range of radius, not all from individual clumps as in pure clumpy torus models. A similar issue has been found for a large sample of quasars (Lyu et al. 2019). Although such models have been popular for fitting torus spectral energy distributions, improvements are needed to make them consistent with the results of reverberation mapping: §4.5.1.

### 5.4. Panel (d), the Sublimation Zone

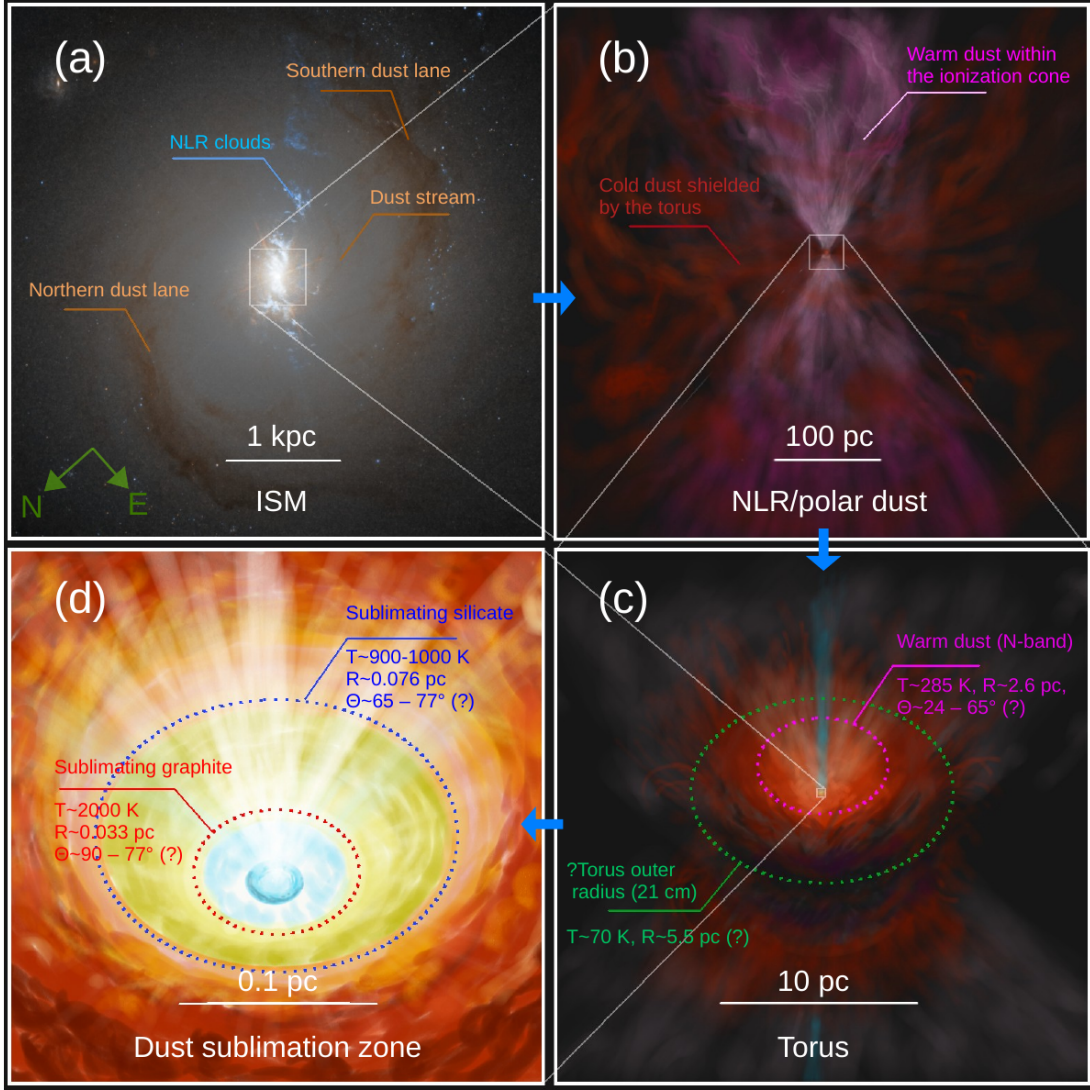


**Figure 20.** Illustration of the circumnuclear dusty environment of NGC 4151 at different scales. Panel (a): The inner 5-kpc region of NGC 4151 as revealed by HST WFC3 images. We can directly see the narrow-line-region (NLR) clouds near the central bright AGN, projecting along two directions, and two dust lanes as well as numerous small dust streams at different locations. Panel (b): Dust components at 100 pc scales, featuring the narrow line region and polar dust in the AGN ionization cone. Outside this cone, relatively cool dust is shielded by the torus from the direct heating of the AGN. Panel (c): Dust structures at  $\sim 1$ –10 pc scales, featuring a flared torus with possible turbulent/outflowing signatures. We denote the torus size constraints in the N-band from our dust reverberation mapping and in the 21cm from radio-band observations in Mundell et al. (2003) (The latter value assumes a system inclination angle of  $45^\circ$ ). Panel (d): The innermost region of the torus over  $\sim 0.01$ –0.1 pc scales, featuring a likely turbulent disk. We have labeled different radii ( $R$ ), dust temperatures ( $T$ ) and ranges of dust half-opening-angles ( $\theta$ ) for sublimations of graphite and silicate dust grains in Panel (d) and AGN warm dust in Panel (c).

- The  $1$ – $4 \mu\text{m}$  torus emission is dominated by carbon and silicate dust, at or close to sublimation temperatures of  $\gtrsim 1500\text{K}$  and  $\sim 900$ – $1000\text{K}$ , and at distances from the central engine of about  $\sim 0.033 \text{ pc}$  and  $\sim 0.076 \text{ pc}$ , respectively: §3.2.4, §4.3. Our finding of two distinct lag times in the near infrared is as predicted by a number of studies (e.g., Baskin & Laor 2018; Swain et al. 2021) and consistent with general expectations given the silicate/carbon composition of interstellar dust.
- The radii of the inner edges of these torus components confirm previous conclusions that the grains are an order of magnitude larger than the small grains in the interstellar medium. Nonetheless, still smaller grains as sublimation products are expected to be stochastically heated and have transient lifetimes, consistent with the relatively high color temperature of the excess between J- and H-bands: §4.4.



- The emission by hot dust in the variable sublimation-temperature component is growing, at  $\sim 4\%$  per year: §3.3.2.
- Underlying the variable emission from the sublimation-temperature dust, there is a relatively non-variable component with a temperature of  $\sim 700\text{K}$ : §3.3.1.
- The inner edge of the torus, identified by the 1500–2500 K dust, does not retreat or otherwise respond significantly to changes in nuclear luminosity on decadal time scales: §3.3.3.
- The robustness of the torus inner edge is consistent with : (1) the sound-speed, which suggests relaxation of the edge should occur only over decadal timescales; and (2) the timescales for destruction of dusty clouds lifted above the torus: §4.6.2

The properties of dust structures in NGC 4151 appear to be generally similar to those for other AGNs and quasars, which have remarkably similar SEDs in the near infrared for  $z \sim 0$ –6 and  $L_{\text{AGN}} \sim 10^8$ – $10^{13} L_{\odot}$  in Lyu & Rieke (2018). From our study of NGC 4151, this similarity probably arises because: (1) the dust composition is dominated by carbon and

silicates, which account for similar portions of the interstellar dust from one AGN to another; (2) the sublimation temperatures place these two dust types at the same temperature regimes regardless of the AGN luminosity; and (3) radiative transfer in the optically-thick circumnuclear tori results in a steep temperature drop beyond the sublimation radius, so the output SEDs resemble each other regardless of details of the torus structure.

## 6. ACKNOWLEDGEMENTS

We thank Tom Soifer for tracking down the origin of a  $11 \mu\text{m}$  measurement, Almudena Alonso-Herrero and Triana Almeyda for comments on the clumpy torus models, Hengxiao Guo for the discussion on the robustness of time lag measurements, Raphael Hviding for feedback on the presentation of this paper. We particularly thank Sebastian Hönig for an extensive discussion. We also thank the referees for their reports. This research has made use of the VizieR catalog access tool, CDS, Strasbourg, France. This work was supported by NASA grants NNX13AD82G and 1255094.

*Software:* Dynesty (Speagle 2020), JAVELIN (Zu et al. 2013), Matplotlib (Hunter 2007), Astropy (Astropy Collaboration et al. 2013, 2018), PyCCF (Peterson et al. 1998; Sun et al. 2018), I<sup>2</sup>CCF (Guo et al. in prep)

## APPENDIX

### A. HOST GALAXY K FLUX

Koshida et al. (2014) quote work by Minezaki et al. (2004) who analyzed images of the galaxy to derive a net host galaxy K-band contribution of  $44.22 \pm 3.83$  mJy in the  $8''.3$  aperture used in the work reported in both papers. Kotilainen et al. (1992) report a detailed analysis of JHK images that should be particularly useful for measuring the galaxy since they were obtained when the nucleus was very faint (Oknyansky et al. 2016). We have started with their measurements in the J band since the contribution of the nucleus is small there. We first subtract their estimate of the nuclear flux (16 mJy) from the averages of all three sets of measurements in the full range of apertures. We then fit the run of J-band flux with aperture diameter with a quadratic (the residuals are negligible) to derive a flux of 77.9 mJy in an  $8''.3$  aperture. Using the standard 2MASS galaxy colors, this value translates into 75.4 mJy at K (using the 2MASS calibration by Cohen et al. (2003)). Taranova & Shenavrin (2013) report two additional estimates of the galaxy contribution, in this case within the  $12''$  aperture used for the SAI photometry. One approach was to assume that the J photometry included only light from the galaxy at the minimum flux. This minimum was at J magnitude 10.73, which translates (using the standard galaxy colors and the aperture effect derived from Kotilainen et al. (1992)) to a K flux density in a  $8''.3$  aperture of  $\sim 66$  mJy. The second estimate is derived by comparing the variations in the various bands and finds the galaxy to be 0.26 magnitudes fainter, leading to a K-band flux of  $\sim 44$  mJy within  $8''.3$ . The deviations in these estimates need to be reconciled.

We therefore made an independent determination of the host galaxy flux. If we make the assumption that the infrared colors of the variable component remain constant and only its amplitude changes (see Taranova & Shenavrin (2013) for a supporting discussion for this case), then the run of  $J - H$  with brightness, e.g. H magnitude, puts tight constraints on both the galaxy flux into the aperture and on the  $J - H$  color of the variable component. The infrared colors of a normal galaxy are critical for this analysis. Fortunately, these colors are virtually independent of galaxy type for ellipticals through mid-type spirals (e.g. Frogel et al. 1978; Persson et al. 1979; Willner et al. 1984; Glass 1984). For the JHK colors, we averaged the values in Persson et al. (1979) and those in Glass (1984), and transformed each to the 2MASS photometric system as in Carpenter (2001). In the first case, the result was  $\langle J - H \rangle = 0.667$  and  $\langle H - K \rangle = 0.238$  with errors of  $\sim 0.01$  and in the second case,  $\langle J - H \rangle = 0.684$  and  $\langle H - K \rangle = 0.242$ , with errors almost as small. We adopted  $\langle J - H \rangle = 0.674$  and  $\langle H - K \rangle = 0.240$ . To compare with the SAI photometry, we used the SAI standard star list (Shenavrin et al. 2011), transformed onto the 2MASS system (next paragraph). Although K-L has less data for deriving transformations, fortunately their accuracy is not critical for our analysis, so we use  $\langle K - L \rangle = 0.25$  from Willner et al. (1984).

The transformations from the SAI JHK photometry to 2MASS were based on the standard stars listed in Shenavrin et al. (2011). These stars are all much too bright to be observed in the unsaturated mode with 2MASS, so they were compared



with heritage photometry from multiple sources, transformed to the 2MASS system as in [Carpenter \(2001\)](#) or with our own transformations of heritage photometry for members of the Bright Star Catalog. The results are:

$$(J - H)_{2\text{MASS}} = (J - H)_{\text{SAI}} + (0.0018 \pm 0.0175) \times (J - H)_{\text{SAI}} + (0.0352 \pm 0.0088) \quad (\text{A1})$$

$$(H - K)_{2\text{MASS}} = (H - K)_{\text{SAI}} + (0.0084 \pm 0.0120) \times (J - K)_{\text{SAI}} + (-0.0084 \pm 0.0074) \quad (\text{A2})$$

$$J_{2\text{MASS}} = J_{\text{SAI}} + (-0.0327 \pm 0.0043) \times (J - K)_{\text{SAI}} + (0.0722 \pm 0.0027) \quad (\text{A3})$$

$$H_{2\text{MASS}} = H_{\text{SAI}} + (-0.0417 \pm 0.0161) \times (J - K)_{\text{SAI}} + (0.0423 \pm 0.0099) \quad (\text{A4})$$

$$K_{2\text{MASS}} = K_{\text{SAI}} + (-0.0399 \pm 0.0073) \times (J - K)_{\text{SAI}} + (0.0533 \pm 0.0045) \quad (\text{A5})$$

The resulting run of  $J - H$  with  $H$  in the 2MASS photometric system is shown as [Figure 1](#) in the main text, where we discuss how it allows an accurate determination host galaxy fluxes at K of  $73 \pm 5$  mJy in the  $12''$  aperture used for the SAI photometry and  $59 \pm 4$  mJy in the  $8.3''$  aperture used in the [Koshida et al. \(2014\)](#) data.

## B. RECONCILIATION OF $10 \mu\text{m}$ MEASUREMENTS

In this section of the appendix, we describe some of the details of the reconciliation of the  $\sim 10 \mu\text{m}$  measurements to a consistent calibration.

There was a series of ‘‘additional observations’’ with IRAS (the normal survey of IRAS did not cover NGC 4151 because of exhaustion of the liquid helium) obtained in June, 1983. The calibration of the additional observations at the flux level of NGC 4151 is uncertain ([Helou & Walker 1988](#)). We averaged two values at  $12 \mu\text{m}$  both derived from these observations: 1.72 Jy ([Sembay et al. 1987](#)) and 2.01 Jy ([Sanders et al. 2003](#)). We subtracted 0.12 Jy as an estimate of the host galaxy contribution, determined by fitting a template SED to the far infrared measurements that are expected to be powered by star formation.

For the test of the photometry, we made use of the *Spitzer* IRS spectrum of the galaxy ([Weedman et al. 2005](#)) both to carry out bandpass corrections to convert measurements in the very broad N filter to the equivalent monochromatic values, and to correct measurements at other wavelengths to  $10.6 \mu\text{m}$ . In all cases where only statistical errors were reported, we added a 7% photometric error by RSS, except in cases where unconventional photometry (e.g., through a scanning slit) suggested larger errors, and in these cases we typically used 10%. The images of [Radomski et al. \(2003\)](#) indicate faint extensions to the nuclear source that account for  $\sim 27\%$  of its  $10.8 \mu\text{m}$  output. We have applied the indicated correction to the measurement by [Soifer et al. \(2003\)](#), consistent with their suggestion. To capture this component, we also re-reduced the imaging results summarized by [Asmus et al. \(2014\)](#) to use aperture photometry with aperture diameters of  $4.62''$  at  $12.6 \mu\text{m}$  and  $3.45''$  at the other bands.

## C. ADDITIONAL FIGURES FROM THE BAYESIAN ANALYSES

In this part of the appendix, we present the outputs of the *Dynesty* Bayesian fitting of the various time lags. These parameters are indicated in appropriate tables in the main text. [Figure 21](#) shows the analysis of the J, H, and L light curves in Interval C relative to the K one. [Figure 22](#) shows similar results for Interval D. Although these latter fits are of lower weight than Interval C due to poorer sampling, they are consistent with the findings for that period. In both cases, we assumed priors for the time lags ( $\Delta t/\text{day} = [-50, 350]$ ). The following two figures illustrate the fits for the infrared lag relative to the B-band light curve, where we assumed the additional prior of the relative optical-to-IR variability amplitude ( $\log \text{AMP} = [-2, 3]$ ) for the two lags.

[Figure 23](#) shows the *Dynesty* results for the lag in Interval C of the individual infrared bands relative to the B-band.

## REFERENCES

- |   |  |
|---|--|
| Alonso-Herrero, A., Quillen, A. C., Rieke, G. H., et al. 2003, <i>AJ</i> , 126, 81  | Allen, D. A. 1976, <i>ApJ</i> , 207, 367   |
| Alonso-Herrero, A., Ramos Almeida, C., Mason, R., et al. 2011, <i>ApJ</i> , 736, 82   | Almeyda, T. R. 2017, ‘‘Dusty donuts: modeling the reverberation response of the circumnuclear dusty torus emission in AGN,’’ Ph.D. thesis, Rochester Institute of Technology |
| Alonso-Herrero, A., Pereira-Santaella, M., Garca-Burillo, S., et al. 2018, <i>ApJ</i> , 859, 144                           | Almeyda, T., Robinson, A., Richmond, M., Vazquez, Billy, & Nikutta, R. 2017, <i>ApJ</i> , 843, 3   |
| Alexander, Tal, Sturm, Eckhard, Lutz, Dieter, Sternberg, Amiel, Netzer, Hagai, Genzel, Reinhard 1999, <i>ApJ</i> , 512, 204 | Almeyda, T., Robinson, A., Richmond, M., Nikutta, R. & McDonough, B. 2020, <i>ApJ</i> , 891, 26  |

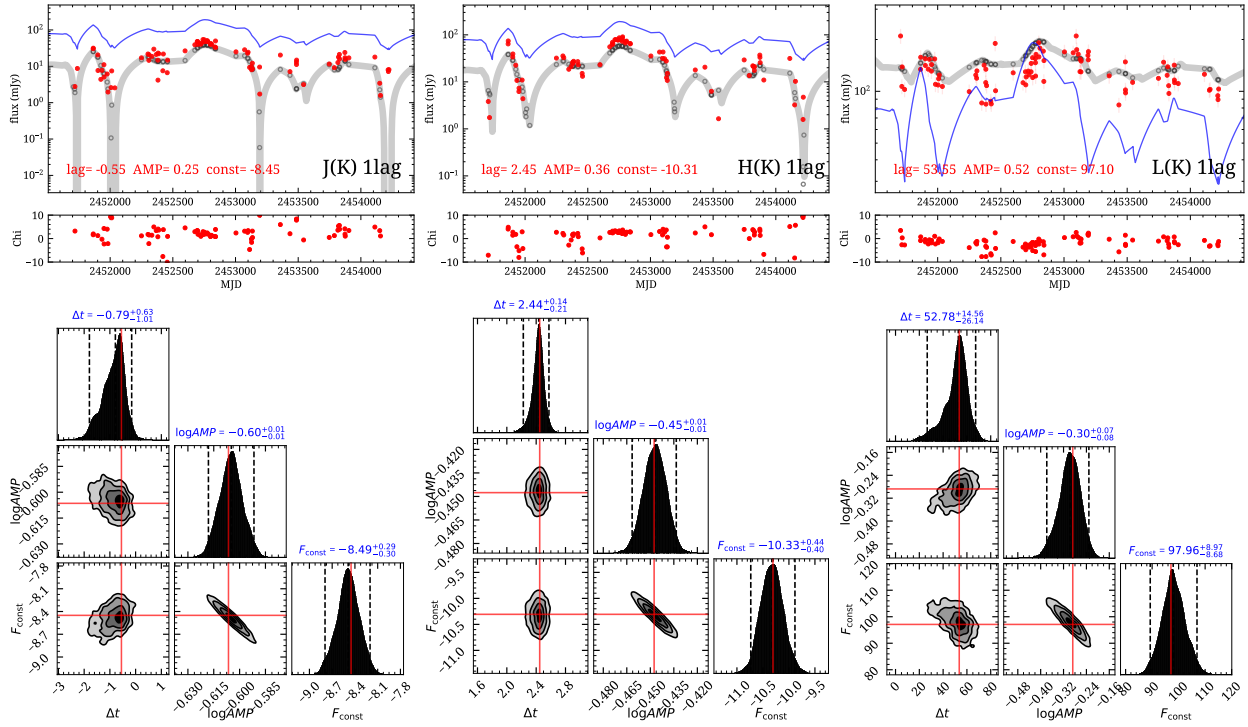


**Figure 21.** Cross-correlation analysis between the J, H, and L light curves to the K-band light curve of NGC 4151 for Interval C. The results for J, H, L bands are shown from left to right. In the top panels, we show the J, K, L light curve data after subtracting the accretion disk variability (and the dust variability traced by K-band subtracted from the L band, based on a  $\sim 1800$  K black body spectrum) as red dots, the best-fit one-lag model as grey thick lines, and the K-band light curve interpolated by a DRW model after subtracting the accretion disk variability as blue thin lines. We denote the value of the best-fit parameters in the MAP sample in red. In the bottom panels, we present the marginalized posterior probability distributions of the fitting parameters, which are the lag time ( $\Delta t$ ), the amplitude of the relevant component (AMP), and a constant term (e.g., a non-variable component,  $F_{const}$ ). On the top of each histogram, we denote the median value of the fitted parameters with 2- $\sigma$  “uncertainties” (i.e., 2.5%, 50% and 97.5% quantiles) that define the 95% confidence intervals in blue. In the probability distribution plots, we use red lines to denote the best-fit values in the MAP sample.

Antonucci, R. 1993, *ARA&A*, 31, 473

Arévalo, P., Uttley, P., Kaspi, S., et al. 2008, *MNRAS*, 389, 1479.  
doi:10.1111/j.1365-2966.2008.13719.x

Asmus, D., Hönig, S. F., Gandhi, P., et al. 2014, *MNRAS*, 439, 1648

Asmus, D., Hönig, S. F., & Gandhi, P. 2016, *ApJ*, 822, 109

Astropy Collaboration, Robitaille, T. P., Tollerud, E. J., et al. 2013, *A&A*, 558, A33. doi:10.1051/0004-6361/201322068

Astropy Collaboration, Price-Whelan, A. M., Sipőcz, B. M., et al. 2018, *AJ*, 156, 123. doi:10.3847/1538-3881/aab4cf

Barvainis, R. 1987, *ApJ*, 320, 537

Barvainis, R. 1992, *ApJ*, 400, 502

Baskin, A., & Laor, A. 2018, *MNRAS*, 474, 1970

Burtscher, L., Jaffe, W., Raban, D., Meisenheimer, K., Tristram, K. R. W., Röttgering, H. 2009, *ApJL*, 705, L53

Burtscher, L., Meisenheimer, K., Tristram, K. R. W. et al. 2013, *A&A*, 558A, 149

Carpenter, J. M. 2001, *AJ*, 121, 2851

Chatterjee, R., Jorstad, S. G., Marscher, A. P., et al. 2008, *ApJ*, 689, 79. doi:10.1086/592598

Clavel, J., Wamsteker, W., & Glass, I. S. 1989, *ApJ*, 337, 236

Crenshaw, D. M., Schmitt, H. R., Kraemer, S. B., et al. 2010, *ApJ*, 708, 419

Cohen, M., Wheaton, Wm. A., and Megeath, S. T. 2003, *AJ*, 126, 1090

Corrales, L. R., García, J., Wilms, J., and Baganoff, F. 2016 *MNRAS*, 458, 1345

Couto, J. D., Kraemer, S. B., Turner, T. J., and Crenshaw, D. M. 2016, *ApJ*, 833, 191

Cutri, R. M., Aitken, D. K., Jones, B., et al. 1981, *ApJ*, 245, 818

Czerny, B., Doroshenko, V. T., Nikolajuk, M., et al. 2003, *MNRAS*, 342, 1222

Das, V., Crenshaw, D. M., Hutchings, J. B. et al. 2005, *AJ*, 130, 945

de Diego, J. A. 2010, *AJ*, 139, 1269.  
doi:10.1088/0004-6256/139/3/1269

Doroshenko, V. T., Lyutyi, V. M., and Shenavrin, V. I. 1998, *Astronomy Letters*, 24, 160

Doroshenko, V. T., Lyuty, V. M., Bochkarev, N. G. et al. 2001, *Ast. Let.*, 27, 65

Draine, B. T., & Lee, H. M. 1984, *ApJ*, 285, 89

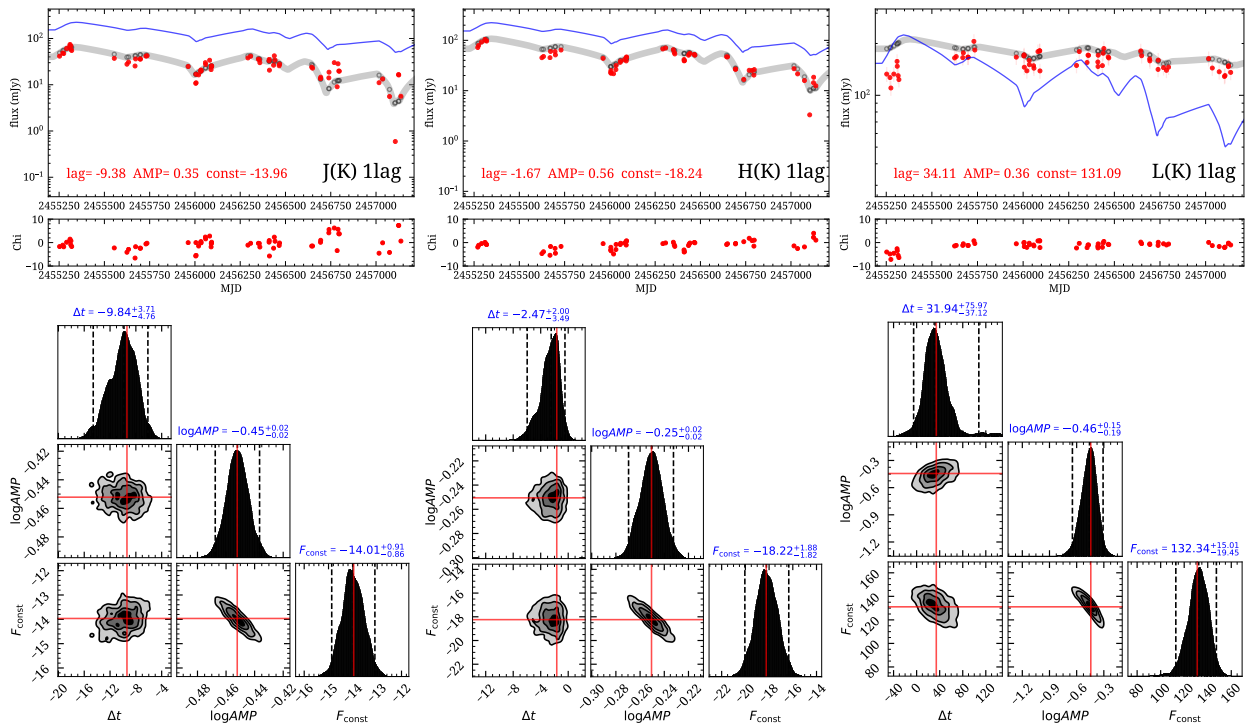
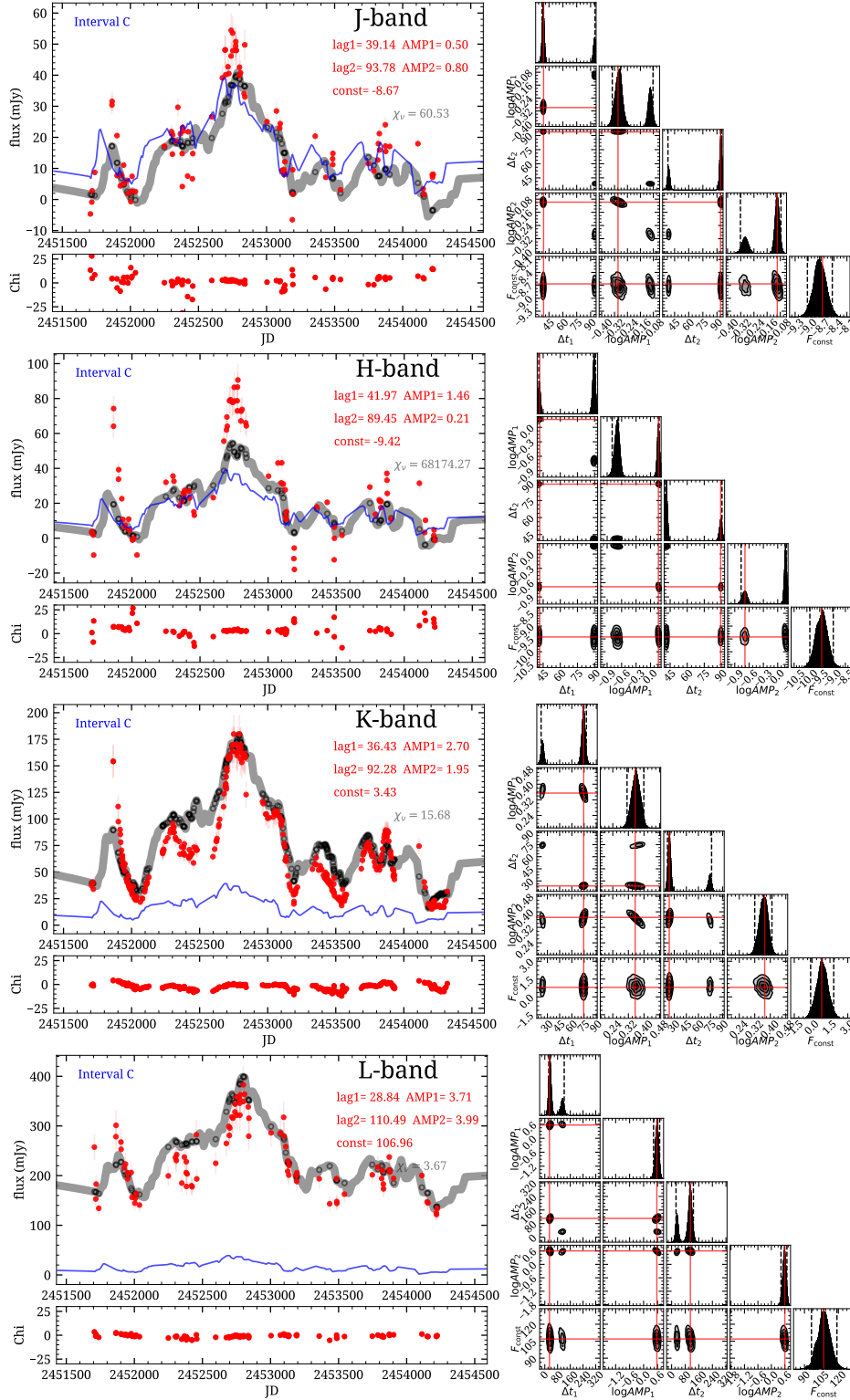


Figure 22. Same as Figure 21, but for Interval D.

- Draine, B. T., & Li Aigen 2001, *ApJ*, 551, 807
- Edelson, R., Gelbord, J., Cackett, E., et al. 2017, *ApJ*, 840, 41
- Efstathiou, A. & Rowan-Robinson, M. 1995, *MNRAS*, 273, 649.  
doi:10.1093/mnras/273.3.649
- Elvis, M., Marengo, M., & Karovska, M. 2002, *ApJL*, 567, L107
- Fischer, T. C., Crenshaw, C. M., Kraemer, S. B. & Schmitt, H. R. 2013, *ApJS*, 209, 1
- Fritz, J., Franceschini, A., & Hatziminaoglou, E. 2006, *MNRAS*, 366, 767
- Frogel, J. A., Persson, S. E., Aaronson, M., and Matthews, K. 1978, *ApJ*, 220, 75
- Fuller, L., Lopez-Rodriguez, E., Packham, C., et al. 2019, *MNRAS*, 483, 3404
- Gallimore, J. F., Elitzur, M., Maiolino, R., et al. 2016, *ApJL*, 829, L7
- García-Bernete, I.; Ramos Almeida, C.; Alonso-Herrero, A. et al. 2019, *MNRAS*, 486, 4917
- García-Burillo, S., Combes, F., Ramos Almeida, C., et al. 2016, *ApJL*, 823, L12
- García-Burillo, S., Combes, F., Ramos Almeida, C., et al. 2019, *A&A*, 632, A61
- Gaskell, C. M. & Klimek, E. S. 2003, *Astronomical and Astrophysical Transactions*, 22, 661
- Gaskell, C. M. 2008, *Revista Mexicana de Astronomia y Astrofisica Conference Series*, 32, 1
- Gaskell, C. Martin and Harrington, P. Z. 2018, *MNRAS*, 478, 1660
- Glass, I. S. 1984, *MNRAS*, 211, 461
- Glass, I. S. 2004, *MNRAS*, 350, 1049
- Greenhill, L. J., Booth, R. S., Ellingsen, S. P., et al. 2003, *ApJ*, 590, 162
- González-Martín, O., Masegosa, J., García-Bernete, I., et al. 2019, *ApJ*, 884, 11
- Gorjian, V., Werner, M. W., Jarrett, T. H., et al. 2004, *ApJ*, 605, 156
- Guo, Z., Aber, J., Garetz, B. A., & Kumar, S. 2002, *J. Quan. Spec. & Rad. Trans.*, 73, 159
- Helou, G., & Walker, D. W. 1988, "IRAS Catalogs and Atlases, Vol. 7: The Amsll Scale Structure Catalog."
- Hernán-Caballero, A., Hatziminaoglou, E., Alonso-Herrero, A., & Mateos, S. 2016 *MNRAS*, 463, 2064
- Hönig, S. F., & Kishimoto, M. 2011, *A&A*, 534, A121
- Hönig, S. F., Kishimoto, M., Tristram, K. R. W., et al. 2013, *ApJ*, 771, 87
- Hönig, S. F., Watson, D., Kishimoto, M., et al. 2014, *Nature*, 515, 528
- Hönig, S. F. & Kishimoto, M. 2017, *ApJL*, 838, L20
- Hönig, S. F. 2019, *ApJ*, 884, 171
- Hopkins, P. F., Hayward, C. C., Narayanan, D., et al. 2012, *MNRAS*, 420, 320
- Horne, K., Peterson, B. M., Collier, S. J. & Netzer, Hagai 2004, *PASP*, 116, 465
- Hunter, J. D. 2007, *Computing in Science and Engineering*, 9, 90
- Ichikawa, K., Packham, C., Ramos Almeida, C., et al. 2015, *ApJ*, 803, 57
- Ichikawa, K. & Tazaki, R. 2017, *ApJ*, 844, 21



**Figure 23.** Two-lag dust reverberation model fitting results of individual IR light curves of NGC 4151 during Interval C (2000/06–2007/05). In the left panels, we show the IR light curve data after subtracting the accretion disk variability as red dots, the best-fit two-lag dust reverberation model as grey thick lines, and the B-band light curve interpolated by a DRW model as blue solid lines. We denote the value of the best-fit parameters in the MAP sample in red. In the right panels, we present the marginalized posterior probability distributions of the fitting parameters. In the probability distribution plots and histogram plots, we use red lines to denote the best-fit values in the MAP sample.



- Imanishi, M., Nakanishi, K., Izumi, T., et al. 2018, *ApJL*, 853, L25
- Kamali, F., Henkel, C., Koyama, S., et al. 2019, *Å*, 624, A42
- Kaspi, S., Maoz, D., Netzer, H., et al. 2005, *ApJ*, 629, 61
- Kawaguchi, T. & Mori, M. 2010, *ApJL*, 724, L183.  
doi:10.1088/2041-8205/724/2/L183
- Kawaguchi, T. & Mori, M. 2011, *ApJ*, 737, 105
- Kemp, J. C., Rieke, G. H., Lebofsky, M. J., & Coyne, G. V. 1977, *ApJL*, 215, 107
- Kishimoto, M., Hönic, S. F., Beckert, T., & Weigelt, G. 2007, *A&A*, 476, 713
- Kishimoto, M., Hönic, S. F., Antonucci, R., et al. 2009, *A&A*, 507, L57
- Kishimoto, M., Hönic, S. F., Antonucci, R., et al. 2011, *A&A*, 527, A121
- Kishimoto, M., Hönic, S. F., Antonucci, R., et al. 2013, *ApJL*, 775, L36
- Kondratko, P. T., Greenhill, L. J., & Moran, J. M. 2005, *ApJ*, 618, 618
- Koshida, S., Yoshii, Y., Kobayashi, Y., et al. 2009, *ApJL*, 700, L109
- Koshida, S., Minesaki, T., Yoshii, Y. et al. 2014, *ApJ*, 788, 159
- Kotilainen, J. K., Ward, M. J., Boisson, C., DePoy, D. L., and Smith, M. G. 1992, *MNRAS*, 256, 149
- Krimm, H. A., Holland, S. T., Corbet, R. H. D., et al. 2013, *ApJS*, 209, 14
- Krolik, J. H. 2007, *ApJ*, 661, 52. doi:10.1086/515432
- Laor, A., & Draine, B. T. 1993, *ApJ*, 402, 441
- Lebofsky, M. J. & Rieke, G. H. 1980, *Nature*, 284, 410
- Levine, A. M., Bradt, Hale, Cui, Wei, Jernigan, J. G. et al. 1996, *ApJL*, 469, 33
- Lyu, J., Rieke, G. H., & Shi, Y. 2017, *ApJ*, 835, 257
- Lyu, J., & Rieke, G. H. 2017, *ApJ*, 841, 76
- Lyu, J., & Rieke, G. H. 2018, *ApJ*, 866, 92
- Lyu, J., Rieke, G. H., & Smith, P. S. 2019, *ApJ*, 886, 33
- Lyuty, V. M., Taranova, O. G., and Shenavrin, V. I. 1998, *Ast. Lett.*, 24, 243
- Lyuty, V. M., and Doroshenko, V. T. 1999, *Ast. Lett.*, 25, 341
- Lyuty, V. M. (2005), *Ast. Lett.*, 31, 645
- Maiolino, R., Marconi, A., & Oliva, E. 2001, *A&A*, 365, 37
- Mann, Ingrid, Murad, Edmond, & Czechowski, Andrzej 2007, *Planet. Space Sci.*, 55, 1000
- Manske, V., & Henning, Th. 1999, *A&A*, 349, 907
- Max-Moerbeck, W., Richards, J. L., Hovatta, T., et al. 2014, *MNRAS*, 445, 437. doi:10.1093/mnras/stu1707
- Manske, V., Henning, T., & Men'shchikov, A. B. 1998, *A&A*, 331, 52
- McAlary, C. W., McLaren, R. A., McGonegal, R. J., & Maza, J. 1983, *ApJS*, 52, 341
- Minezaki, T., Yoshii, Y., Kobayashi, Y., et al. 2004, *ApJL*, 600, L35
- Minezaki, T., Yoshii, Y., Kobayashi, Y., et al. 2019, *ApJ*, 886, 150
- Mor, Rivay, Netzer, Hagai, & Elitzur, Moshe 2009, *ApJ*, 705, 298
- Mou, G., Wang, T., & Yang, C. 2017, *ApJ*, 844, 30
- Mundell, C. G., Wrobel, J. M., Pedlar, A., et al. 2003, *ApJ*, 583, 192
- Namekata, D., Umemura, M., & Hasegawa, K. 2014, *MNRAS*, 443, 2018
- Nenkova, M., Sirocky, M. M., Ivezić, A., & Elitzur, M. 2008a *ApJ*, 685, 147
- Nenkova, M., Sirocky, M. M., Nikutta, R., Ivezić, A., & Elitzur, M. 2008b *ApJ*, 685, 160
- Netzer, H. 2015, *ARA&A*, 53, 365
- Netzer, H. 1987, *MNRAS*, 225, 55
- Noda, H., Kawamuro, T., Kokubo, M., et al. 2020, *MNRAS*, 495, 2921
- O'Dell, S. L., Puschell, J. J., Stein, W. A., & Warner, J. W. 1978, *ApJS*, 38, 267
- Oknyanskii, V. L. 1993, *Astronomy Letters*, 19, 416
- Oknyanskij, V. L., Lyuty, V. M., Taranova, O. G., et al. 1999, *Astronomy Letters*, 25, 483
- Oknyanskij, V. L. & Horne, K. 2001, *Probing the Physics of Active Galactic Nuclei*, 224, 149
- Oknyanskij, V. L., Lyuty, V. M., Taranova, O. G., et al. 2006, *AGN Variability from X-Rays to Radio Waves*, 360, 75
- Oknyanskij, V. L., Metlova, N. V., Artamonov, B. P. et al. 2013, *Odessa Ast. Pub.*, 26, 212
- Oknyansky, V. L., Gaskell, C. M., & Shimanovskaya, E. V. 2015, *Odessa Astronomical Publications*, 28, 175
- Oknyansky, V. L., Metlova, N. V., Taranova, O. G., et al. 2014, *Astronomy Letters*, 40, 527
- Oknyansky, V. L., Gaskell, C. M., & Shimanovskaya, E. V. 2015, *Odessa Astronomical Publications*, 28, 175
- Oknyanskij, V. L., Metlova, N. V., Huseynov, N. A., Guo, Di-Fu, and Lyuty, V. M. 2016, *Odessa Ast. Pub.*, 29, 95
- Oknyansky, V. L., Shenavrin, V. I., Metlova, N. V., and Gaskell, C. M. 2018, *Odessa Ast. Pub.*, 30, 94
- Oknyansky, V. L., Shenavrin, V. I., Metlova, N. V., and Gaskell, C. M. 2019, *Astronomy Letters*, 45, 197
- Persson, S. E., Frogel, J. A., and Aaronson, M. 1979, *ApJS*, 39, 61
- Peterson, B. M., Pogge, R. W., Wanders, I., Smith, Sean M., and Romanishin, W. 1995, *PASP*, 107, 579
- Peterson, B. M., Wanders, I., Horne, K., et al. 1998, *PASP*, 110, 660. doi:10.1086/316177
- Pott, J.-U., Malkan, M. A., Elitzur, M., et al. 2010, *ApJ*, 715, 736
- Puccetti, S., Fiore, F., Risaliti, G., et al. 2007, *MNRAS*, 377, 607
- Raban, D., Jaffe, W., Röttgering, H., Meisenheimer, K., & Tristram, K. R. W. 2009, *MNRAS*, 394, 1325
- Radomski, J. T., Piña, R. K., Packham, C., et al. 2003, *ApJ*, 587, 117
- Ramos Almeida, C., Levenson, N. A., Rodríguez Espinosa, J. M., et al. 2009, *ApJ*, 702, 1127

- Ramos Almeida, C., Levenson, N. A., Alonso-Herrero, A., et al. 2011, *ApJ*, 731, 92
- Ramos Almeida, C., & Ricci, C. 2017, *Nature Astronomy*, 1, 679
- Richards, G. T., Lacy, M., Storrie-Lombardi, L. J., et al. 2006, *ApJS*, 166, 470
- Rieke, G. H. 1978, *ApJ*, 226, 550
- Rieke, G. H., & Low, F. J. 1975, *ApJL*, 200, 67
- Rieke, G. H., & Lebofsky, M. J. 1981, *ApJ*, 250, 87
- Rieke, G. H., Alonso-Herrero, A., Weinere, B. J. et al. 2009, *ApJ*, 692, 556
- Risaliti, G. & Elvis, M. 2004, *Supermassive Black Holes in the Distant Universe*, 187
- Roberts, C. A., & Rumstay, K. R. 2012, *Journal of the Southeastern Association for Research in Astronomy*, 6, 47
- Sanders, D. B., Mazzarella, J. M., Kim, D.-C., Surace, J. A., & Soifer, B. T. 2003, *AJ*, 126, 1607
- Schartmann, M., Wada, K., Prieto, M. A., Burkert, A., & Tristram, K. R. W. 2014, *MNRAS*, 445, 3878
- Schmitt, H. R., Antonucci, R. R. J., Ulvestad, J. S., et al. 2001, *ApJ*, 555, 663
- Schnülle, K., Pott, J.-U., Rix, H.-W., et al. 2013, *A&A*, 557, L13
- Schnülle, K., Pott, J.-U., Rix, H.-W., et al. 2015, *A&A*, 578, A57
- Schurch, N. J., Warwick, R. S., Griffiths, R. E., and Kahn, S. M. 2004, *MNRAS*, 350, 1
- Sembay, S., Hanson, C. G., & Coe, M. J. 1987, *MNRAS*, 226, 137
- Sergeev, S. G., Doroshenko, V. T., Golubinskiy, Yu. V. et al. 2005, *ApJ*, 622, 129
- Shapovalova, A. I., Popović, L. Č., Burenkov, A. N., et al. 2010, *A&A*, 509, A106
- Shenavrin, V. I., Taranova, O. G., and Nadzhip, A. E. 2011, *Ast. Reports*, 55, 31
- Shomshekova, S. A., Denissyuk, E. K., Valiullin, R. R. et al. 2019, *Astrophysics*, 62, 163
- Siebenmorgen, R., Heymann, F., & Efstathiou, A. 2015, *A&A*, 583, A120
- Soifer, B. T., Bock J. J., Marsh, K. et al. 2003, *AJ*, 126, 143
- Speagle, J. S. 2020, *MNRAS*, 493, 3132
- Stalevski, M., Ricci, C., Ueda, Y., et al. 2016, *MNRAS*, 458, 2288
- Stalevski, M., Frtiz, J., Baes, M., Nakos, T., & Popović, L. C. 2011, *MNRAS*, 420, 2756
- Stein, W. A., & Weedman, D. W. 1976, *ApJ*, 205, 44
- Sturm, E., Alexander, T., Lutz, D., et al. 1999, *ApJ*, 512, 197
- Suganuma, M., Yoshii, Y., Kobayashi, Y., et al. 2006, *ApJ*, 639, 46
- Sun, M., Grier, C. J., & Peterson, B. M. 2018, *Astrophysics Source Code Library*. ascl:1805.032
- Swain, S., Shalima, P., Latha, K. V. P., & Swamy, K. B. S. 2021, *arXiv2102.04662v1*
- Taranova, O. G., and Shenavrin, V. I. 2013, *Ast. Reports*, 57, 71 (originally in *Astronomicheskii Zhurnal*, 90, 91, 2013)
- Urry, C. M. & Padovani, P. 1995, *PASP*, 107, 803
- Uttley, P., Edelson, R., McHardy, I. M., et al. 2003, *ApJL*, 584, L53. doi:10.1086/373887
- van Velzen, S., Gezari, Suvi, Hammerstein, Erica, Roth, Nathaniel, Frederick, Sara. et al. 2020, *arXiv 2001.01409 v1*
- Vazquez, Billy 2015, "Constraining the size of the dusty torus in active galactic nuclei," Ph.D. thesis, Rochester Institute of Technology
- Venanzi, Marta, Hönic, S. F., & Williamson, D. 2020, *ApJ*, 900, 174
- Wada, K. 2012, *ApJ*, 758, 66
- Wang, Ye, Ferland, Gary J., Hu, Chen, Wang, Jian-Min, and Du, Pu 2012, *MNRAS*, 424, 2255
- Wang, J.-M., Du, P., Brotherton, M. S., et al. 2017, *Nature Astronomy*, 1, 775
- Ward, M., Elvis, M., Fabbiano, G., et al. 1987, *ApJ*, 315, 74
- Weedman, D. W., Hao, Lei, Higdon, S. J. U. et al. 2005, *ApJ*, 633, 706
- Weingartner, J. C. & Draine, B. T. 2001, *ApJ*, 548, 296
- Wheeler, J. C. 1990, "Introduction of Supernovae," in *6. Jerusalem Winter School for Theoretical Physics: Supernovae*, ed. T. Piran, S. Weinberg, J. C. Wheeler; Singapore: World Scientific Publishing, pp 1 - 93
- Williamson, D., Hönic, S., and Venanzi, M. 2020, *ApJ*, 907, 26
- Willner, S. P., Ward, M., Longmore, A. et al. 1984, *PASP*, 96, 143
- Yuan, W., Fausnaugh, M. M., Hoffmann, S. L., et al. 2020, *ApJ*, 902, 26. doi:10.3847/1538-4357/abb377
- Zu, Y., Kochanek, C. S., Kozłowski, S., & Udalski, A. 2013, *ApJ*, 765, 106